METAL DEPOSITS ON THIN WELL ORDERED OXIDE FILMS: MORPHOLOGY, ADSORPTION AND REACTIVITY

M. BÄUMER, J. LIBUDA, and H.-J. FREUND
Fritz-Haber-Institut der Max-Planck-Gesellschaft
Faradayweg 4-6, 14195 Berlin, Germany

Work on clean oxide surfaces, such as NiO, CoO, FeO, Cr_2O_3 and Al_2O_3, where adsorption and reaction of small molecules has been studied, is reviewed. The studies on the clean surfaces are the basis for investigations of transition metal particles deposited onto these oxide surfaces: Ag, Pd, Rh and Pt have been deposited on thin alumina films and the morphology has been determined via STM and SPA-LEED. Photoelectron spectroscopy was applied to investigate the electronic structure of the deposits as a function of particle size. The bonding between molecules and the metal aggregates has been characterized via thermal desorption spectroscopy and x-ray absorption spectroscopy. We find a considerable variation of adsorption strength as a function of particle size and the kind of metal. Additionally, examples for size dependent reactivity are presented.

1. Introduction

Disperse metal catalysts play an important role in several technically important reactions [1-3]. Sometimes the yield and selectivity of such reactions depend on the average size of the metal particles involved, i. e. the reaction is size selective. Examples are the hydrogenolysis of ethane and the oxidation of carbon monoxide [4]. Very often the catalysts are prepared by choosing an appropriate support material, such as SiO_2, Al_2O_3 or MgO, and depositing a transition metal compound onto the support surface from solution or by chemical vapour deposition. Via calcination and subsequent reduction, metal deposits are formed on the support surface.

Several groups have recently started to model such systems by depositing a metal from the vapour onto single crystal oxide surfaces for investigations under ultra-high vacuum conditions [5-10]. Most of them have used bulk single crystals as support materials [11-44]. However, thin films of corresponding oxides have also been employed which were prepared on top of a metal substrate [45-73]. Such systems have several experimental advantages over bulk single crystal surfaces. For instance, charging of the sample under electron bombardment or during electron spectroscopic measurements are completely avoided. Also, cooling of the surface to low temperatures in rather short times is achieved via the intimate contact between the oxide film and the metallic

substrate, whereas the often found low heat conductances hamper effective cooling of bulk materials. By controlling the thickness of the film, an electronic structure of the formed oxide may be established which is representative of its bulk electronic structure [47]. In addition, thin films may be prepared with different surface crystallographic orientations, a task which is considerably more difficult for bulk single crystals [8,9]. In particular, the preparation of polar surfaces of ionic systems is very difficult via cleavage of bulk crystals due to the very high surface energies of these systems [74].

In the following, we review some results from our laboratory on adsorption and re-action on clean metal oxide surfaces in an introductory chapter, and then dwell more specifically on results of metal deposits on a model alumina surface. Especially, we ad-dress the morphology of the metal deposits for different transition metals and then dis-cuss the electronic structure as studied by photoelectron and other electron spectroscopies. Finally, we report on the interaction of the metal deposits and discuss associative and dissociative adsorption. Specific emphasis will be placed onto those properties which are strongly dependent on the size of the deposited metal particle.

2. Analytical Tools and Oxide Preparation

The experiments were performed in several ultrahigh-vacuum systems which are equipped with various surface science tools. The methods available are: photoemission (XPS, ARUPS), electron energy loss spectroscopy (ELS, HREELS), thermal desorption spectroscopy (TDS), Auger electron spectroscopy (AES), infra-red reflection absorp-tion spectroscopy (IRAS), and electron spin resonance spectroscopy (ESR) [75-77]. We have investigated both, bulk single crystals cleaved in vacuo as well as in situ prepared thin oxide films. The typical preparation methods for the thin films are summarized in Fig. 1. The first one is the simple oxidation of the corresponding metal single crystal surface, applying high oxygen dosages coupled with heating cycles. If there is a large lattice mismatch between the metal and the native oxide, as it is the case of NiO/Ni, the film exhibits a rather pronounced defect density. While this may be of interest in itself if one wants to study the influence of surface defects on adsorption, it is also de-sirable to prepare films with a very small defect density. This is possible via the choice of an appropriate metal substrate with a lattice spacing that fits the oxide lattice spac-ings [21,60]. The metal to be oxidized is then evaporated onto the inert substrate either in an oxygen atmosphere or it is oxidized after deposition. In the case of a NiO(100) film, for example, a Ag(100) surface may be used as substrate. For the preparation of a NiO(111) film, Au(111) is an appropriate substrate [59]. Another attractive technique, as presented in the third panel, is the oxidation of alloy single crystals. We have used this alternative to prepare a well-ordered Al_2O_3 film [78-83]. The advantage here is the high melting point of the alloy which allows heating of the film to high temperatures and in turn leads to ordering within the film. In contrast to this situation, oxidation of an Al metal substrate would not lead to an ordered film, because Al would melt before
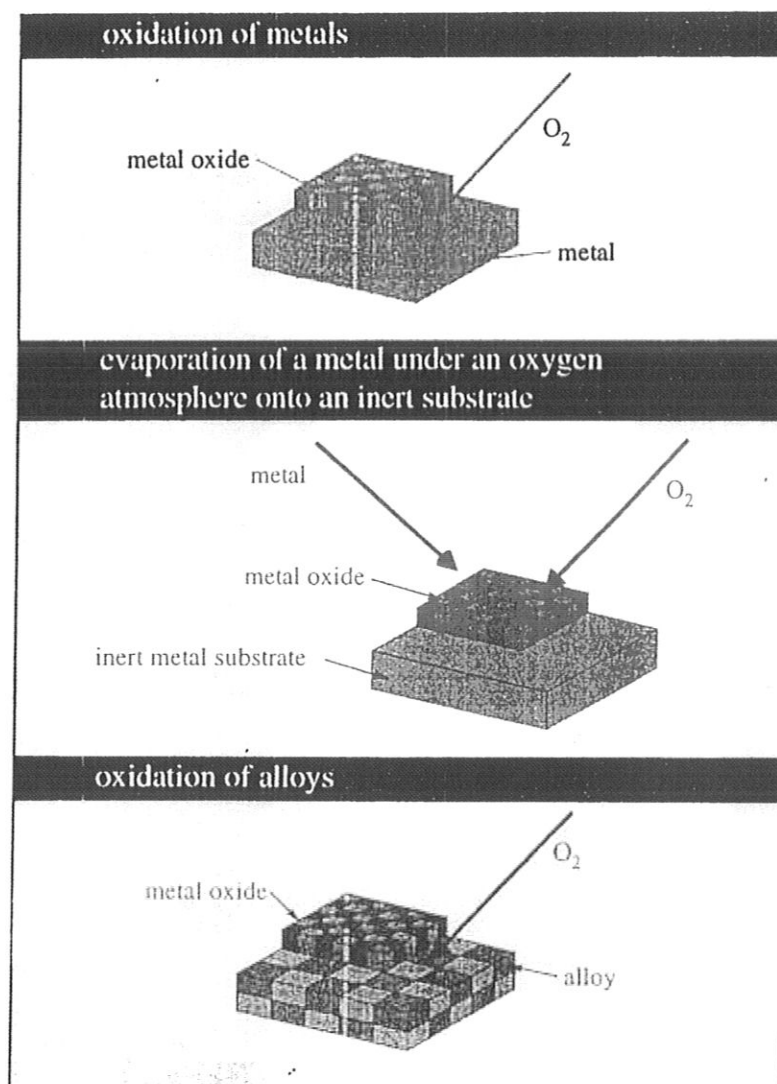
Figure 1. Methods for thin oxide film preparation.

Al_2O_3 orders. Choosing NiAl(110) as a substrate for Al_2O_3 also assures that the Ni, set free in the oxidation process, is dissolved in the bulk of the alloy because Ni_3Al is the thermodynamically favourable alloy stoichiometry so that the bulk of the alloy tries to enrich with Ni.

3. Structure and Reactivity of Clean and Modified Oxide Surfaces

Structure and reactivity of oxide surfaces may vary considerably depending on the system. We have studied rock salt type surfaces as well as corundum type surfaces, nonpolar and polar surfaces, oxides that are reactive, like NiO or Cr_2O_3 for example, and oxides which are inert, such as Al_2O_3 [74]. The clean oxide surfaces as well as those modified by deposition of alkali [63, 84, 85] have been investigated. In the following,

we shall present results on a chemically reactive polar $Cr_2O_3(0001)$ surface and compare with a chemically inert but isostructural Al_2O_3 surface.

Before we turn to the explicit examples, we briefly summarize our results on other oxide surfaces. We have investigated a series of oxides with rock salt structure, i.e. NiO, CoO, and FeO [49, 74]. The question around which our research centred was the electronic and structural stability of the polar (111) faces. Vibrational spectroscopy (HREELS) was used to show that the apparently non-reconstructed (111) surfaces were hydroxyl terminated [55]. The OH termination effectively reduces the surface charge and stabilizes the surface. Upon removal of the hydroxyls as water by a thermal treatment, the surface becomes unstable and undergoes reconstruction [86, 89]. The particular reconstruction found on the ionic surfaces has been termed the octopolar reconstruction because the formation of octopolar units is found at the surface exposing microfacets with (100) orientation. Only the topmost atom of each of the octopolar units is still in a coordination typical for a (111) surface, while all other atoms are in the typical fivefold (100) coordination. The surface energy of such a reconstructed surface is still considerably higher (4.38 Jm^{-2}) compared to the (100) surface (1.38 Jm^{-2}) and the hydroxyl terminated non-reconstructed surface [90]. This energy content may be used to drive chemical reactions. In fact, the reconstructed surface does interact much stronger with adsorbed molecules as compared with the hydroxyl terminated or the non-reconstructed (100) surfaces. Papp and coworkers [91] have recently demonstrated that topotactically prepared NiO powder, preferentially exposing (111) surface planes, indeed exhibits higher activity in deNOx-reactions and that its reactivity is correlated with the water content of the powder.

Parallel to the work on polar surfaces, we have studied the adsorption properties of the non-polar (100) surface [52]. The ideal surface, containing no defects, adsorbs CO with rather small binding energy of about 0.2...0.3 eV [51]. The bond is almost exclusively electrostatic in nature and due to the interaction of the multipolar moment of the (100) surface with the quadrupol moment of CO, whose dipole moment is very small [3, 92-98]. However, the small interaction is large enough to orient the molecule on the surface in such a way that the carbon atom points towards the Ni cation and the axis is oriented perpendicularly with respect to the surface plane. For NO the binding energy is slightly larger, i.e. 0.4...0.5 eV, and there are indications from vibrational spectra [53] as well as from other observations that a small covalent contribution has to be considered [3, 92-98]. It is this small covalent contribution that leads to an orientation of the molecule with the nitrogen atom towards a Ni ion in the surface and an inclined axis with respect to the surface normal (45°). The NO stretching vibration is red shifted [53] with respect to the gasphase indicating a slight additional population of the 2π-antibonding NO orbital via interaction with the surface. In the case of CO, on the other hand, there is a very small blue shift of the vibrational stretching frequency indicative of the so called wall-effect [92], where a non chemically bonded molecule vibrates towards a heavy wall. Water only physisorbs on the NiO(100) surface as long as

the surface is perfect. Upon creation of defects, however, the behaviour becomes more similar to the polar surface in the sense that water spontaneously dissociates and hydroxyl groups are formed on the surface [50]. These hydroxyl groups are readily observed in vibrational spectra and proved via isotopic labelling with heavy water [50]. Spectroscopic identification of terrace sites on the surface is possible with electron energy loss spectroscopy. We have shown [74, 99] that the coordinatively unsaturated Ni ions in the surface exhibit typical electronic d-d excitations which are energetically shifted with respect to those of the octahedrally coordinated Ni ions in the second and deeper layers. Since the ligand field of a surface Ni ion changes when a molecule is coordinated to it, these d-d excitations are energetically further shifted upon adsorption. This observation may be used to identify adsorption sites. It has been demonstrated that differently coordinated Ni ions in the surface lead to different d-d excitations [49]. Coming back to the dissociation of water on NiO defects, addressed above, we can follow the process in the EL-spectra [8]. Since water only dissociates at the defect sites, the d-d excitations typical for the terrace sites are not influenced by the hydroxyl groups formed in the dissociation process.

The $Cr_2O_3(0001)$ surface is a polar surface as well, and, therefore - according to theoretical predictions -, we have to expect strong structural relaxations. In fact, a recent LEED I/V analysis [67] together with other spectroscopic evidences [62, 64] have clearly revealed that the surface is very far from being bulk terminated. Two possibilities for the bulk terminated surface are shown in Fig. 2a. Ion scattering spectrocopy (ISS) [62] indicates, however, the presence of only half the number of chromium ions on the surface. Electron energy loss spectroscopy of the d-d excitations [64] may be used to clearly determine the oxidation state of the chromium ions as Cr^{3+}. Therefore, in order to depolarize and thus stabilize the surface, the distribution of metal ions in the surface is likely to be as shown in Fig. 2b. This is actually the situation also corroborated by the LEED structure analysis [67]. In addition, however, the interlayer distances relax considerably. The surface chromium ions are pulled into the surface oxygen layer, and the buckling of the chromium ion layer just beneath the first oxygen plane is reduced. Even more than four layers beneath the surface interlayer relaxation can be observed. This relaxed $Cr_2O_3(0001)$ surface is still chemically very active. We have investigated adsorption of various molecules, such as O_2, CO, C_2H_4, H_2O, and also metallic adsorbates such as Na [62-67, 85]. We only want to mention that CO adsorption leads to a non-classic side-on coordination [66], similar to ethene which is classically [68, 69, 70] side-on coordinated. Under ultrahigh vacuum conditions adsorption is fully reversible in both cases. Upon raising the pressure to 1 bar, however, it is possible to polymerize ethene at slightly elevated temperature.

In contrast to the polar NiO(111) surface, the $Cr_2O_3(0001)$ surface does not readily dissociate water. The reason is clear: the surface is stabilized by removal of half of the metal ions and additional relaxations to such an extend that the surface energy is comparable to the non-polar surfaces. Thus, dissociative adsorption of water will not lead
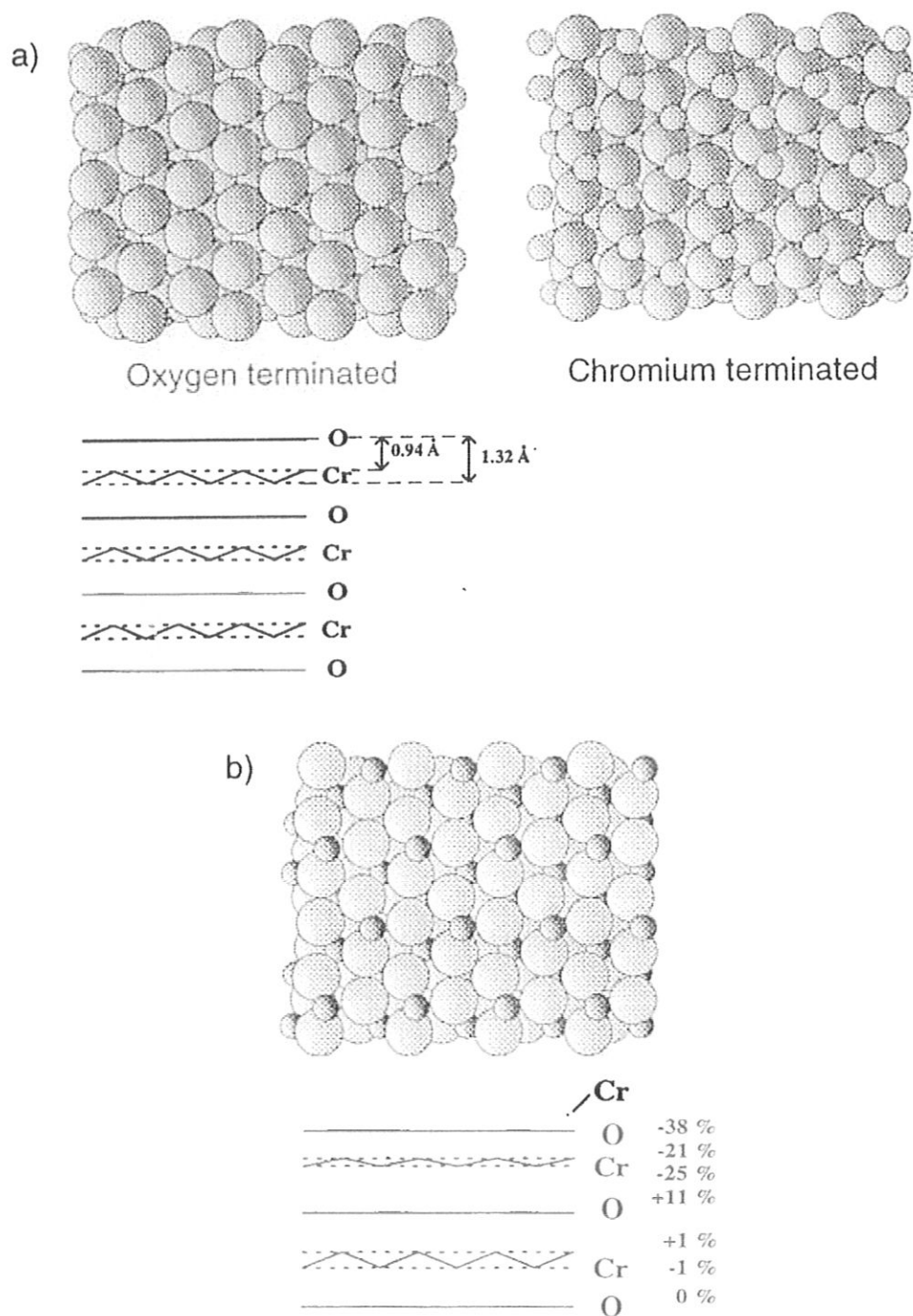
a)

Oxygen terminated   Chromium terminated

$$
\begin{array}{ll}
\rule{3cm}{0.4pt}\ O^- & \updownarrow 0.94\,\text{Å} \quad \updownarrow 1.32\,\text{Å} \\
\sim\!\sim\!\sim\!\sim\ Cr & \\
\rule{3cm}{0.4pt}\ O & \\
\sim\!\sim\!\sim\!\sim\ Cr & \\
\rule{3cm}{0.4pt}\ O & \\
\sim\!\sim\!\sim\!\sim\ Cr & \\
\rule{3cm}{0.4pt}\ O &
\end{array}
$$

b)

/Cr	
O	-38 %
Cr	-21 %
	-25 %
O	+11 %
	+1 %
Cr	-1 %
O	0 %

Figure 2. a) Possible terminations of the $Cr_2O_3(0001)$ surface. Termination by a complete layer of oxygen ions (left) and by a complete layer of chromium ions (right). Bottom: stacking of layers (schematically). b) Reconstructed and depolarized $Cr_2O_3(0001)$-surface (top) and inter-layer distances after reconstruction (bottom).

to further stabilization. It is possible to dissociate water via photoinduced processes [50]. At this point we would like to consider oxygen adsorption in somewhat more detail because it also allows us to understand how the oxide film grows on the surface. We shall mainly use results from infra-red reflection absorption spectroscopy [68, 70].
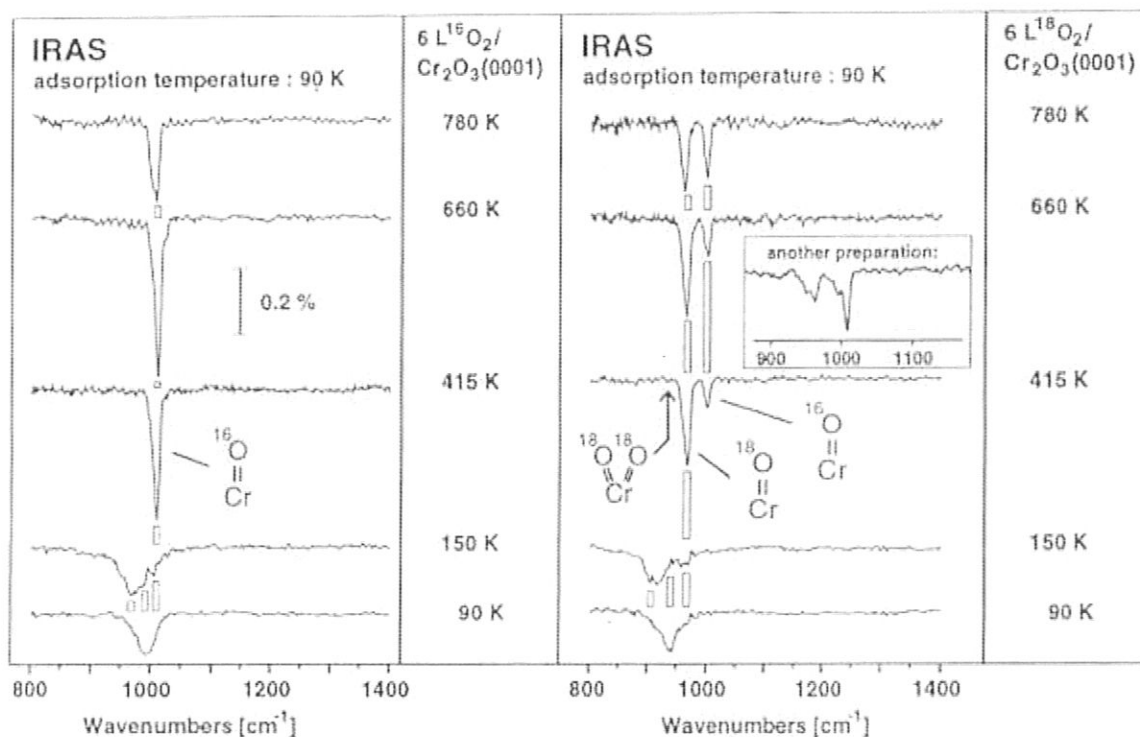
Figure 3. Infrared spectra of a $Cr_2{}^{16}O_3(0001)$-surface after dosing of 6 L $^{16}O_2$ (left) and 6 L $^{18}O_2$ (right) at 90 K and subsequent heating to given temperatures.

Figure 3 shows a set of infra-red spectra taken after dosing 6 L at 90 K and subsequent heating to temperatures between 90 K and 780 K. On the left hand side spectra obtained after dosing $^{16}O_2$, on the right hand side those obtained after dosing $^{18}O_2$ are depicted. At lowest temperature a broad peak centred around 990 cm^{-1} ($^{16}O_2$) and 930 cm^{-1} ($^{18}O_2$), respectively, shows up. While there is only little intensity at 965 cm^{-1} ($^{16}O_2$) and 905 cm^{-1} ($^{18}O_2$), this intensity increases to form another broad band as the surface temperature rises to 150 K. At this temperature or a little below, another spectral feature, finally developing into a rather sharp peak, starts to show up at 1005 cm^{-1} ($^{16}O_2$) and at 960 cm^{-1} ($^{18}O_2$). For the $^{16}O_2$ dosage, a single relatively sharp feature grows until the surface reaches a temperature of 660 K. Then it starts to decrease again. In the case of $^{18}O_2$ dosage, two sharp features at 960 cm^{-1} and 1005 cm^{-1} are observed. The peak at 1005 cm^{-1} gains intensity as the temperature increases. Depending somewhat on the preparation conditions of the Cr_2O_3 film, the sharp feature may be split by approximately 10 cm^{-1} as shown in the inset and published earlier [69]. Also, all measured frequencies are compatible with the previously published HREELS data [62]. We note at this point that the oxide film was grown using $^{16}O_2$, i.e. before the adsorption experiments were carried out. If the oxide film is grown using $^{18}O_2$, the infra-red spectra after adsorption of oxygen $^{16}O_2$ or $^{18}O_2$, respectively, did not show any difference in comparison to the spectra from the $Cr_2{}^{16}O_3$ film. On the basis of the TD-spectra not shown here it is quite obvious that the broad features observed below 150 K to 220 K are due to

molecular adsorbed O_2. In fact, it is probably the feature with maximal intensity at 965 cm^{-1} ($^{16}O_2$) and 905 cm^{-1} ($^{18}O_2$), becoming more prominent in the IRA-spectra after heating to 150 K, that leads to a strong desorption feature at 300 K. The higher frequency peak at 990 cm^{-1} ($^{16}O_2$) and 930 cm^{-1} ($^{18}O_2$) could be associated with the O_2 molecules desorbing at lower temperature, indicative for a smaller interaction with the substrate. The shift can also be due to the change in intermolecular interaction. The adsorbed molecular species show a stretching frequency rather different from the gas phase value (1554.7 cm^{-1}) [85]. The frequency shifts with respect to the gas phase are similar to those observed for peroxo- or superoxo-compounds [100, 101], nominally containing an O_2^{2-} or an O_2^{-} moiety. While Cr 2p XPS data indicate a charge transfer from the surface [62] to the O_2 moiety, this charge transfer has to be rather small as revealed by electronic ELS data [69]. The data are compatible with an O_2 molecule moderately (covalently) interacting with the substrate and inducing only a small charge transfer. This would also be consistent with an oxygen molecule that leads to an O-O vibrational absorption in the region around 1000 cm^{-1}. It is important to note, of course, that upon heating above room temperature the transitions in the EL-spectrum (see [68, 69]) disappear but the Cr^{3+} surface excitations do not reappear indicating that there is still surface oxygen present. Effectively, the oxidation state of the surface chromium ions has increased after dissociation. This surface oxygen gives rise to the sharp feature in the IRA-spectra. The observed frequency is typical for Cr=O bonds as found in chromyl compounds [102]. The isotope shift for Cr=O is smaller as compared with the isotope shift for $^{18}O_2$ / $^{16}O_2$ adsorption. The fact that for certain conditions the Cr-O vibrational mode is split (see Fig. 3) is compatible with two different mono-oxo Cr=O species on the surface, whose relative concentrations would depend on preparation conditions. However, it would also be consistent with a CrO_2 species as in CrO_2Cl_2 with two Cr=O bonds at one chromium ion. In fact, the observed split is very close to the difference between the in- and out-of-phase coupled stretching normal modes of CrO_2Cl_2 as mentioned above. The present isotopic labelling data reveal instead the existence of single Cr=O bonds as discussed in the following: Consider again Fig. 3 and let us assume for the moment that the vibration at 1005 cm^{-1} is due to ^{16}O-Cr-^{16}O as in CrO_2Cl_2. If we expose a $Cr_2^{16}O_3(0001)$ surface with $^{18}O_2$, we would have to expect the formation of ^{18}O-Cr-^{18}O, ^{18}O-Cr-^{16}O and ^{16}O-Cr-^{16}O of the adsorbed dissociated oxygen, because it may exchange with the lattice oxygen. Indeed, as the temperature is increased, the right hand side of Fig. 3 indicates the formation of a second band, but a third band has never been observed under these conditions. The frequency of the first band (1005 cm^{-1}) occurring after adsorption of $^{18}O_2$ is identical to the one found for $^{16}O_2$ exposure. Since we assumed within the present argument that this band is due to ^{16}O-Cr-^{16}O with two Cr=^{16}O bonds, the observation of only two bands would indicate that there is no ^{18}O-Cr-^{18}O species which is unreasonable from a statistical point of view. The position of the expected ^{18}O-Cr-^{18}O mode is shown in Fig. 3. Therefore, we come to the conclusion that dissociation of O_2 leads to the formation of chromyl species
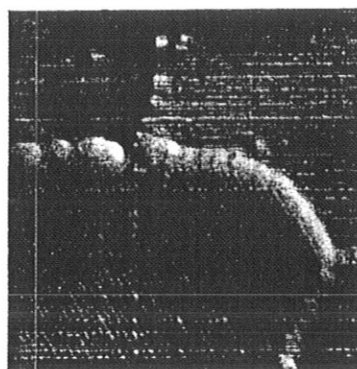
Figure 4. STM image (CCT, constant current topography, 500 Å× 500 Å, +4 V, 2 nA) of the growing Al_2O_3 film (patch with diagonal lines) near NiAl step edges [112].

with single Cr=O bonds on the surface similar to the situation found for polycrystalline samples [103-106].

While oxygen slightly withdraws charge from the surface, alkali is expected to enrich the electron density at the surface. This has, indeed, been observed [68]. Na grows on $Cr_2O_3(0001)$ in a Frank-van der Merwe mode very similar to its growth on a metal surface [63]. The full sodium layer is metallic and very effectively screens the strong Fuchs-Kliewer phonons of the dielectric substrate when excited with electrons. At sub-monolayer coverage there are two sodium species on the surface [68], namely an ionic as well as a neutral species, with the neutral species appearing beyond half a monolayer. Once the ionic species is formed, charge is injected into the surface, and the EL-spectra indicate the formation of a Cr^{2+} species on the surface [68]. We have shown [68, 69] that bonding of molecules such as ethene is different on the alkali free and the alkali predosed surface. It may be interesting to note that on the basis of bulk thermodynamic data we would predict a reduction of Cr_2O_3 to Cr metal by sodium. However, this did not happen under any circumstances tried. Earth alkali metals such as Mg, on the other hand, easily reduce Cr_2O_3 to Cr metal via formation of MgO [107]. With Na we may reduce NiO to Ni metal and simultaneously form sodiumoxide [89]. Other, more stable oxides, such as Al_2O_3 may not be reduced by Na. However, Na may be incorporated into the bulk of some oxides [108] as we have observed for Cr_2O_3 [68].

Al_2O_3 in its α–form is isostructural with Cr_2O_3. As mentioned above, a thin Al_2O_3 film may be formed via oxidation of a NiAl(110) single crystal surface. A STM picture of the growing film is shown in Fig. 4. The film is only 5 Å thick as revealed via XPS [109] and Auger data [110]. Eventually, it covers the surface completely growing even across steps of the metallic substrate like a carpet [111]. Such kinds of growth modes are well known from alkali halide epitaxy on elemental semiconductor surfaces [111]. ISS has been used to show that the surface is mainly oxygen terminated [131]. With photoelectron spectroscopy the two dimensional band structure of the film has been
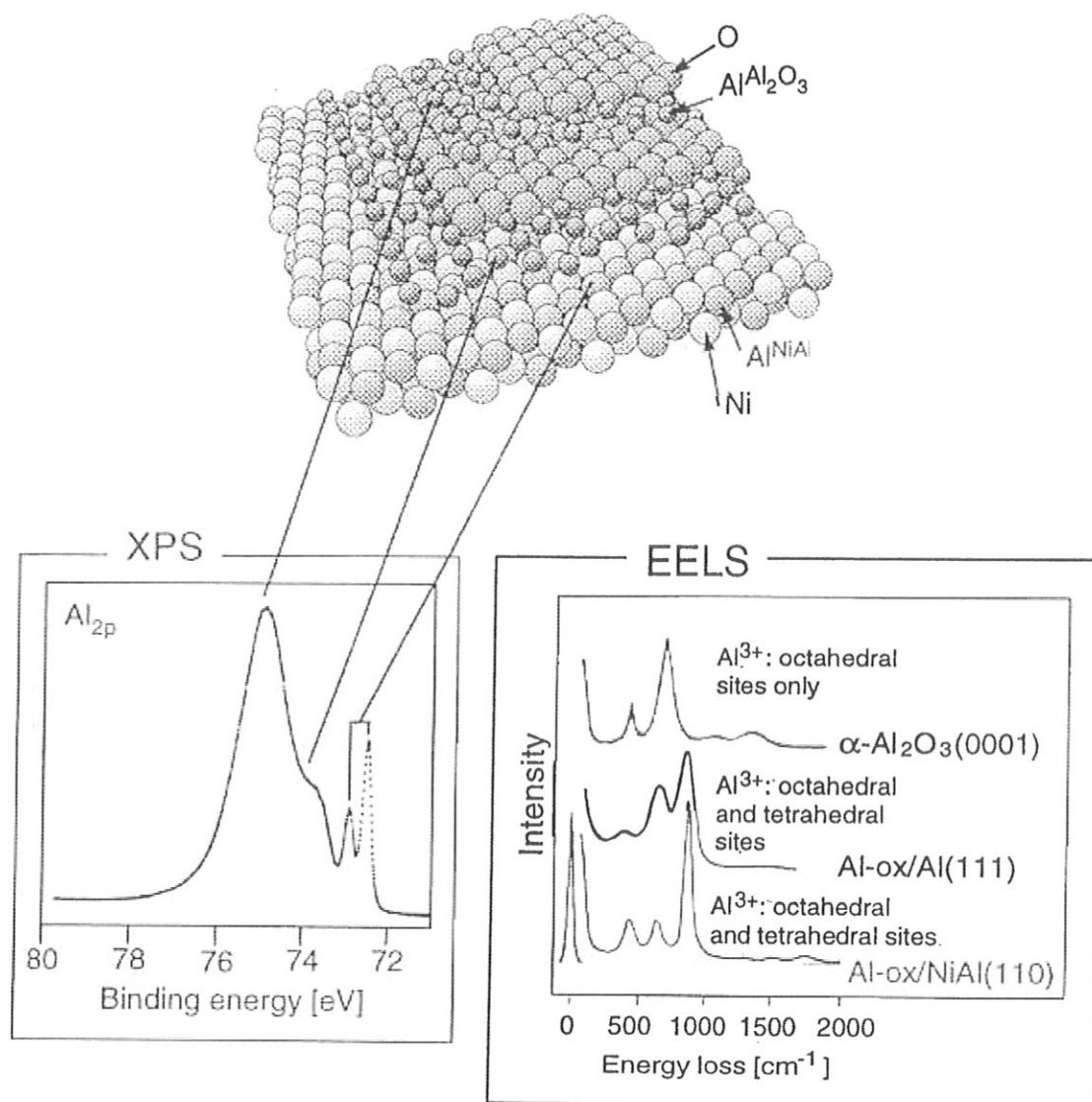
Figure 5. Left: Al 2p photoelectron spectum of Al₂O₃/NiAl(110) (hv = 150 eV, normal emission). Substrate-, interface- and oxide components are clearly resolved.
Right: High resolution electron energy loss spectra of various Al₂O₃ surfaces.

measured [78], and this is compatible with a hexagonal arrangement of oxygen atoms in the oxide film. XPS may be used to identify the coordination of the aluminium ions in the film [109]. Figure 5 shows an Al 2p spectrum of the film. The sharp double peak at lowest binding energy can clearly be assigned to ionization of Al in the alloy substrate. The shoulder at 74 eV turns out to be due to Al located at the interface between the substrate and the oxide film. The broad band at highest binding energy results from ionization of the Al ions sandwiched between the oxygen layers. However, from the spectra it is not possible to differentiate between Al ions tetrahedrally or octahedrally coordinated, because the inherent line widths are too large. Here the phonon spectrum, also shown in Fig. 5, helps in the assignment [78]. The fact that the spectrum exhibits
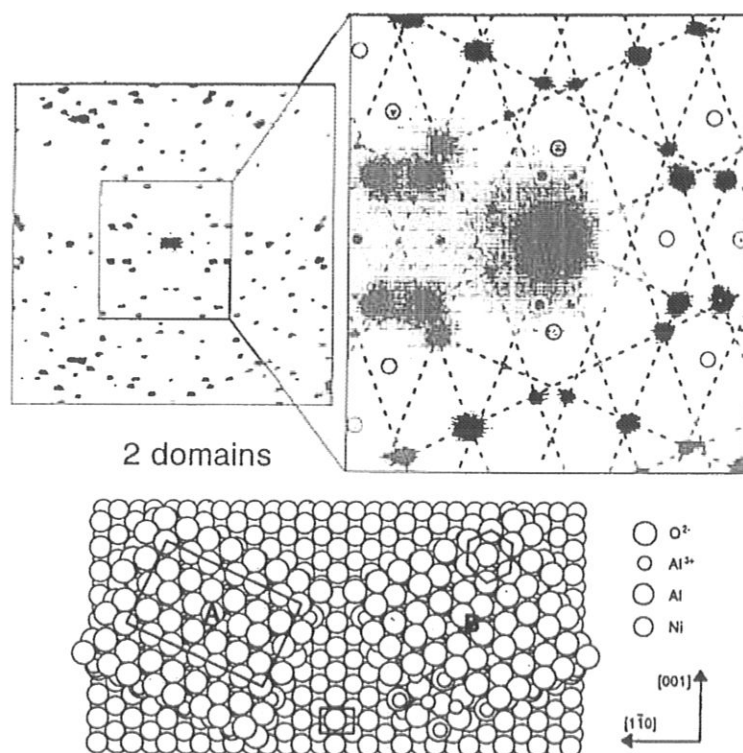
Figure 6. Top: LEED pattern (85 eV) of Al_2O_3/NiAl(110) and close-up of an area around the (00)-spot. In addition to the substrate and oxide spots (the oxide lattice is indicated by dashed lines) the incommensurability of the oxide superstructure gives rise to a number of double diffraction spots indicated in the close-up. Bottom: Structure model of Al_2O_3/NiAl(110), derived from a distorted γ-Al_2O_3 structure. The unit cell as derived from the LEED pattern is indicated.

three phonon bands is indicative of the presence of both tetrahedrally and octahedrally coordinated aluminium ions: α-Al_2O_3 which only contains octahedrally coordinated Al ions exhibits a phonon spectrum with two bands while γ-Al_2O_3 with ions in both coordinations exhibits a three band spectrum similar to the present film. The electron diffraction diagram indicates a very high degree of order in the film as shown in Fig. 6. The LEED pattern may be interpreted to arise from the superposition of two domains which are rotated by 42° with respect to each other [82]. The domains are commensurate with the substrate in the (110) direction and incommensurate in the direction perpendicular to this, i.e. (100). A typical defect on the Al_2O_3 film forms where the two domains intersect. Figure 7 shows a STM picture of such a domain boundary. Another defect observed on the film results from antiphase domain boundaries which form within one domain by a lateral shift of areas with identical rotational orientation on the surface. These antiphase domain boundaries may be detected via a detailed LEED spot profile analysis but can also be directly observed via STM as a white line pattern visible in Fig. 8 [83]. We shall see in the following that these defects may act as nucleation centres for metal particle growth on the surface [112-123]. Unfortunately, the STM topographs shown in Fig. 7 and Fig. 8 do not reveal atomic resolution of the
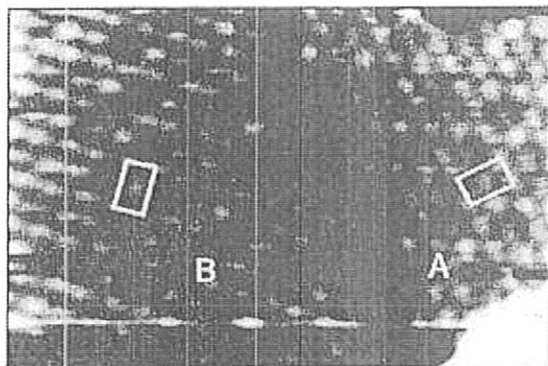
Figure 7. STM image (CCT, 210 Å× 130 Å, -2 V, 0.5 nA) of Al$_2$O$_3$/NiAl(110). Domains of orientation A and B can be observed, the unit cells are indicated.

Figure 8. STM image (CCT, 500 Å× 500 Å, 4 V, 0.5 nA) of Al$_2$O$_3$/NiAl(110) showing several anti-phase boundaries.

oxide film. The reason is the rather high tunnelling voltage which is neccessary because the smallest energy to tunnel from the oxide density of states into the STM tip is near 4 eV. At such a high voltage the tip has to be retracted from the surface so far that atomic resolution is lost. If we lower the tunneling voltage we may tunnel from the metal substrate underneath the oxide film into the tip [83]. Via this procedure, it is possible to image the interface between the alloy substrate and the oxide film as shown in Fig. 9. With the low tunnelling voltages applied, it is now even possible to achieve atomic resolution. The schematic diagram indicates how we interpret this topograph. It seems that the substrate accomodates the incommensurate oxide film by slightly shifting every fourth atom in the rows across the surface, oriented according to the angle of rotation of the domain. On the basis of these experimental results, we have a rather detailed picture of the morphology of the alumina film.
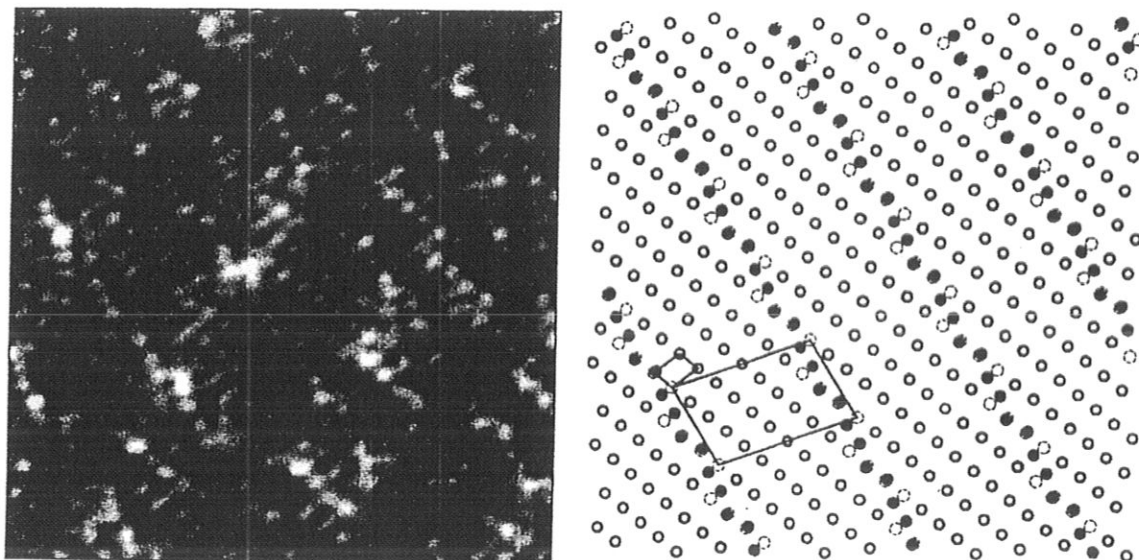
Figure 9. STM image (CCT, 90 Å× 90 Å, -1 V, 1.5 nA) of Al_2O_3/NiAl(110) showing the structure of the NiAl(110) interface in atomic resolution.

With respect to the chemistry of the alumina film, we find that it is rather inert with respect to molecules like CO and O_2 [80, 81]. Figure 10 contains EL spectra of CO adsorbed on the surface at low temperature [80]. The thermal desorption spectra also shown indicate that we need temperatures below 80 K to adsorb appreciable quantities of CO on the surface. The electronic EL spectra exhibit vibrational fine structure in the excited state and excitation energies very close to the gas phase values, indicating that the coupling between the molecule and the surface is rather weak. The coupling, however, is not weak for all molecules. While O_2 behaves similar to CO, other free radicals such as NO, NO_2 and, in particular, di-tert-butyl-nitroxide (DTBN) show pronounced interaction with the surface [124]. We have studied the interaction of the latter moelcule in detail via a newly designed UHV-ESR spectrometer and refer to the literature [124]. At low temperature, we observe a strong coupling of the spin on the free radical probably with Al ions in the surface. This seems at first sight to be in contradiction to the oxygen termination observed via ISS. However, if we consider the strong surface relaxations observed for the Cr_2O_3 surface, where the Cr and oxygen ions are almost in one plane at the surface, it is quite conceivable that a similar effect allows for the interaction between the lower layers and the molecules on top. Therefore, we may state that the question whether the Al_2O_3 surface will participate in the surface chemistry strongly depends on the molecules involved. In this respect, our alumina film behaves very similar to a typical alumina support material used in catalytic modelling. There are, however, differences. In particular, interaction of the film with water is rather weak. In fact, the film is - within the detection limit - free of hydroxyl groups. This, on the one hand, is very unusual because real alumina surfaces always carry hydroxyl groups [78-83]. On the other hand, this is a desirable property
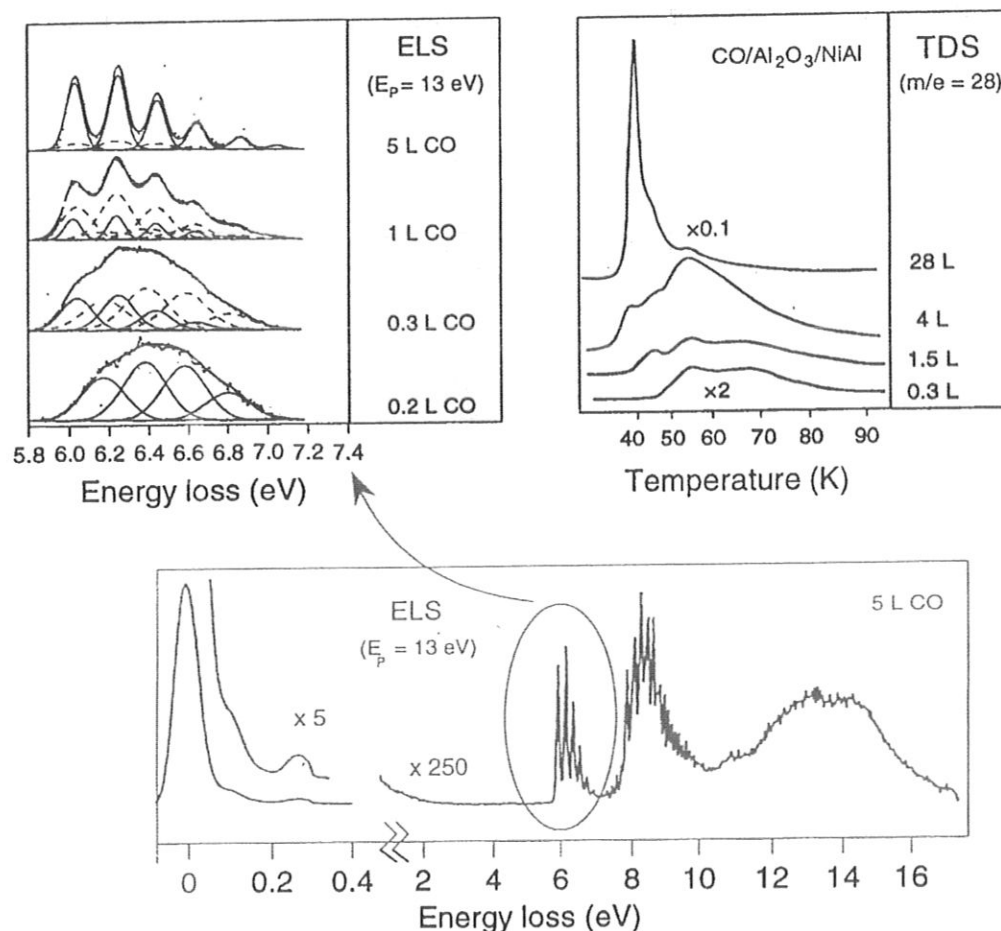
Figure 10. Electron energy loss spectrum for CO/Al₂O₃/NiAl(110) (bottom).
Left: Close-up of the region indicated. Right: Thermal desorption spectra for CO/Al₂O₃/NiAl(110).

because it allows us to study directly the influence of adsorbed hydroxyl groups if we could manage to specifically hydroxylate the film. This, indeed, may be achieved as indicated in Fig. 11. At the top (A), the Al 2p spectra of the clean oxide film obtained with electron detection normal to the surface (left hand side) and grazing detection (right hand side) are shown [3, 112]. In the next set of spectra (B), the clean oxide film has been dosed with Al from an evaporation source and covered with less than a mono-layer of the metal. The Al signal shows up particularly at grazing detection. The further step (C) involves the treatment of the evaporated aluminium with water in oder to form aluminium hydroxide at the surface leading to the disappearence of the me-tallic aluminium signal. At the same time there appears a characteristic shoulder in the O 1s spectrum, also shown, which is indicative of the formation of surface hydroxyl groups. The same procedure may also be used to grow a thicker aluminium oxide film, if, instead of water, oxygen is used for oxidation.
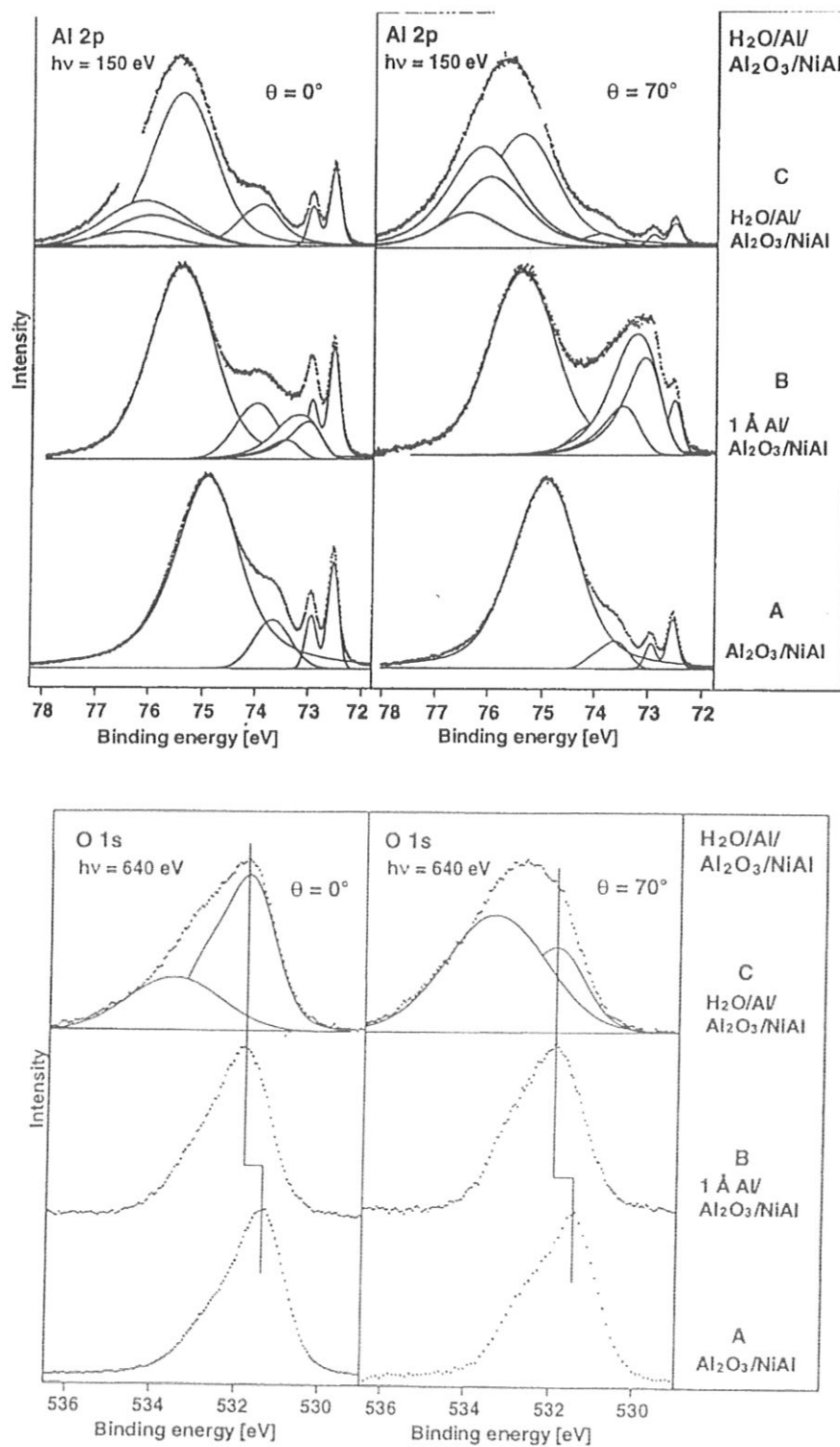
Figure 11. Al 2p (a) and O 1s (b) core level spectra for the chemically modified Al$_2$O$_3$/NiAl(110) surface.
A: Clean Al$_2$O$_3$/NiAl(110). B: Deposition of 1 Å Al at 300 K.
C: After H$_2$O exposure at 90 K and subsequent heating to 300 K.

4.   Morphology and Electronic Structure of Metals on Oxide Surfaces

By deposition of additional chemical components, we may start to modify the above discussed oxide surfaces. We focus here on modification by evaporation of ultrathin metal films. As alluded to in the introduction we may consider such systems as model systems for disperse metal catalysts. Typical examples for supported metals are those where a transition metal is deposited onto a support such as SiO_2, Al_2O_3 or MgO. MgO [51, 125, 129] and Al_2O_3 [78-83, 130-132] have been prepared as well-ordered thin film supports. As far as the preparation of well-ordered thin SiO_2 films is concerned, there are still problems. We have concentrated on the preparation of alumina films of the type discussed in the previous chapter including the possibilities of chemical func-tualisation before metal deposition. In the following, we shall dwell on growth, morphology and electronic structure of such films.

Figure 12 shows a set of STM pictures of metal deposits onto the clean, chemically unmodified alumina surface. For the picture on the top, 1/3 of a monolayer of Ag has been deposited [114]. In the middle panel and on the bottom almost equal amounts of Rh [133] and Pt [112] have been evaporated onto this substrate, which was at room temperature in all three cases. Obviously, Ag has a very high mobility at room temperature and, consequently, rather large aggregates form, which nucleate at the very few steps of the alumina film. In the case of Rh, the mobility is still pronounced but less than in the case of Ag. The metal moves across the alumina terraces but only reaches the antiphase domain boundary defects. Pt exhibits the lowest mobility among the three examples, which is documented by its nucleation directly on the terraces. The relevant quantities that determine the adsorption energy (E_{ads}) of the metal on the substrate are connected via the classical Young equation [134-136]:

$$E_{ads} = E_{oxide/gas} + E_{metal/gas} - E_{oxide/metal} \qquad (1)$$

where the first two terms referring to the oxide/gas and metal/gas interactions may be estimated, while the third term, referring to the metal/oxide interaction, is generally not known. Whether metal particles move at a given temperature, now strongly depends on E_{ads}. If $E_{ads} < 0$, the metal wets the surface, and we observe a layer-by-layer or Frank-van der Merwe growth mode. Provided that $E_{ads} > 0$, we find the formation of three-dimensional islands (Volmer-Weber-growth). Sometimes an intitial layer-by-layer growth mode is followed by three-dimensional growth at a given layer thickness. This is called a Stranski-Krastanov growth mode [136]. Of course, as is documented by Fig. 12, the detailed defect structure of the substrate is as important for the finally observed morphology as the strength of interaction with the ideal substrate. While in the case of Ag only the steps on the alumina surface exhibit sufficient interaction strength at room temperature to nucleate Ag particles, the interaction of Rh with the
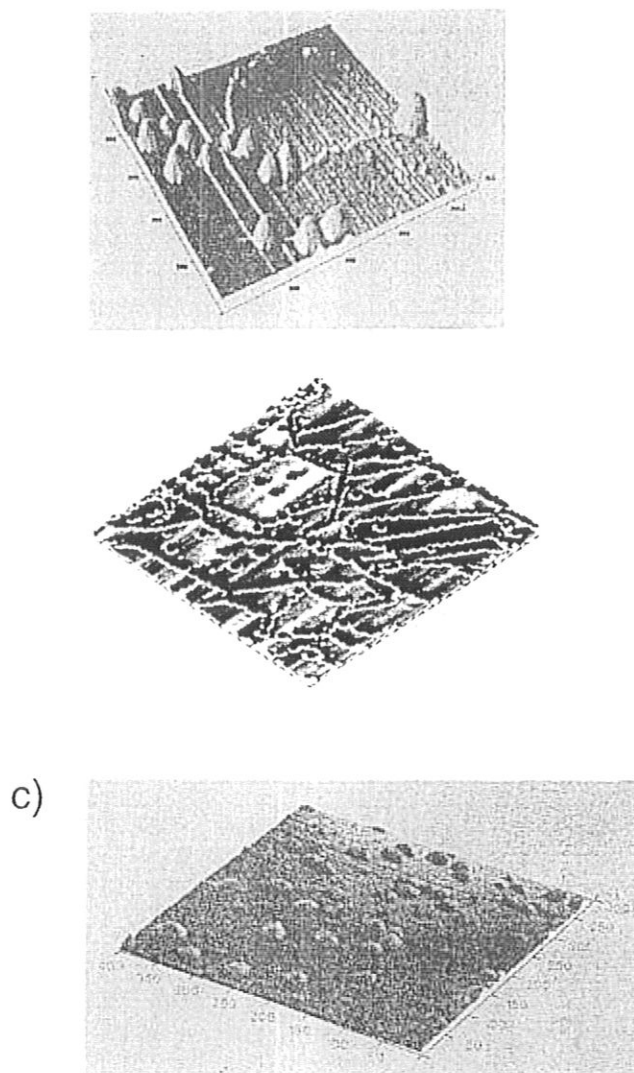
Figure 12. STM images of Al₂O₃/NiAl(110) after metal deposition:
a) Growth of Ag at 300 K (CCT, 900 Å× 900 Å, -0.6 V, 0.5 nA).
b) Growth of Rh at 300 K (CCT, 1500 Å× 1500 Å, +3 V, 1.6 nA).
c) Growth of Pt at 300 K (CCT, 400 Å× 400 Å, -4 V, 0.8 nA).

antiphase domain boundaries is strong enough to lead to nucleation at those defects [113, 126]. Another example, which we want to discuss in more detail in the following, shows nucleation and growth modes being intermediate between Pt and Rh. Figure 13 shows STM topographs of Pd deposited at 90 K (Fig. 13a) and at room temperature (Fig. 13b) [118]. Pd deposited at 90 K decorates the antiphase domain boundaries but also nucleates on the terraces, probably at point defects. In the case of deposition at room temperature, considerably larger aggregates are formed due to the higher mobility in the deposition process. There is no particular preference of formation at defects or on the terraces. The aggregates imaged in Fig. 13b partly exhibit the shape of small crystallites. The crystallographic orientation of the metal particle planes are revealed from electron diffraction diagrams as shown in Fig. 13c [118]. The oxide reflexes are
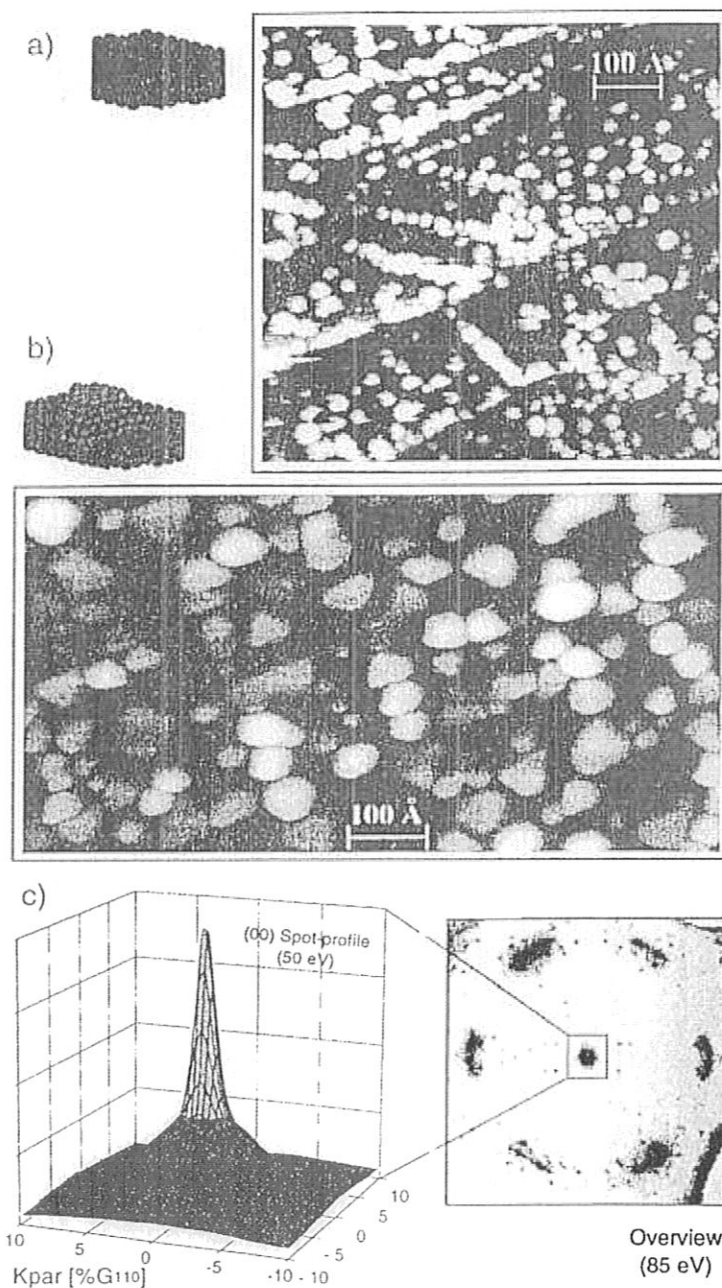
Figure 13. Pd growth on Al_2O_3/NiAl(110): a) STM image after Pd deposition at 90 K (CCT, 1.6 V, 2.2 nA). b) STM image after Pd deposition at 300 K (CCT, +0.4 V, 0.5 nA). c) LEED pattern after deposition of 20 Å Pd at 300 K (right) and intensity profile of an area close to the (00)-spot (left).

superimposed by two diffuse, but clearly visible, hexagonal (111) oriented LEED patterns which are rotated by 12° with respect to each other. The two rings result from growth on the two domains of the alumina substrate. An analysis of the LEED spot profiles yields detailed conclusions on the average metal island size, the average island separation, as well as of the island density and the number of atoms per island. Figure 14 shows as an example the (0,0) profile after Pd deposition at both temperatures.
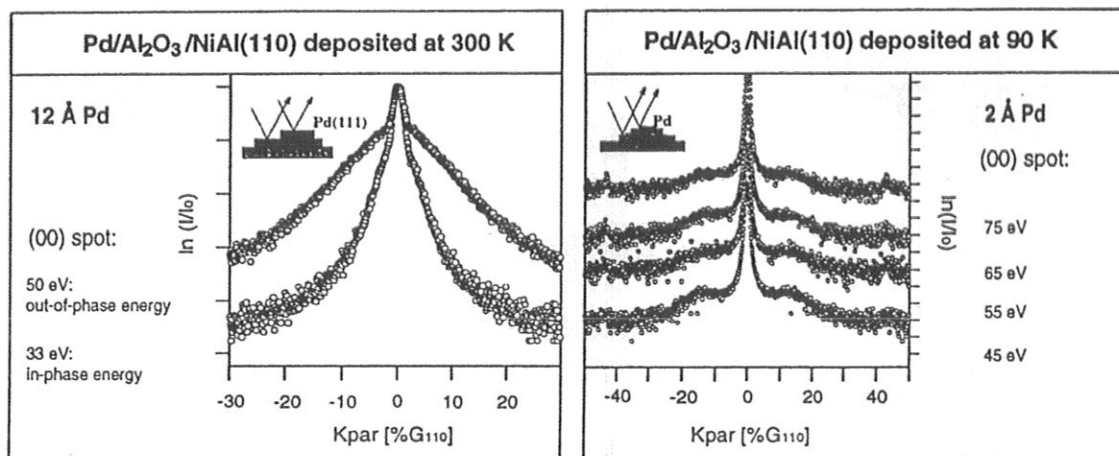
Figure 14. LEED spot intensity profile of the (00)-reflex at various electron energies after deposition of Pd on Al₂O₃/NiAl(110). Left: Pd growth at 300 K. Right: Growth at 90 K.

Shoulders are particularly emphasized if a logarithmic intensity scale is chosen. From the shape and the intensity variation of the shoulder as a function of the electron energy, a rather well documented analysis [137, 138] allows the desired information to be extracted. Figure 15 shows the island size as a function of the amount of deposited material as determined via a quartz microbalance. For 300 K, the island size reaches a plateau after a relatively steep ascent. At this point, equilibrium between nucleation, diffusion and growth is reached. Only if more than 12-15 Å material is deposited, the average island size increases via coalescence of smaller islands very rapidly. The islands then have a regular shape with well-ordered crystallographic planes. This shows up in the energy dependence in Fig. 14 (left hand side), where clear in-phase and out-of-phase relations among the scattered electron beams from the various terraces of the growing aggregate are detected. Such energy dependences are not found for the deposit prepared at 90 K (right hand side). Obviously, island growth is considerably different from the room temperature case. Probably due to the reduced mobility during evaporation, the typical merging into a plateau region cannot be detected. Figure 15 compares the island densities and numbers of atoms per island and shows the expected strong increase in island density in the range of 10 Å layer thickness for room temperature deposition. Apparently, many of the islands do not form at the beginning of the growth process by heterogeneous nucleation at preferential sites but rather at a later point in the process by homogeneous nucleation or nucleation at weakly preferential sites. The analysis of the number of atoms per island leads to similar conclusions. Note that even at low coverages the formation of aggregates with more than 1000 atoms is found. At 90 K deposition temperature, the situation changes significantly. We observe a high island density of (10^{13} cm^{-2}) already at very low coverages. Coalescence sets in at an early stage and leads to a steady decrease of island density. Consequently, the number of atoms per aggregate varies over a large range, indicating that under these circumstances very small as well as very large islands are accessible.
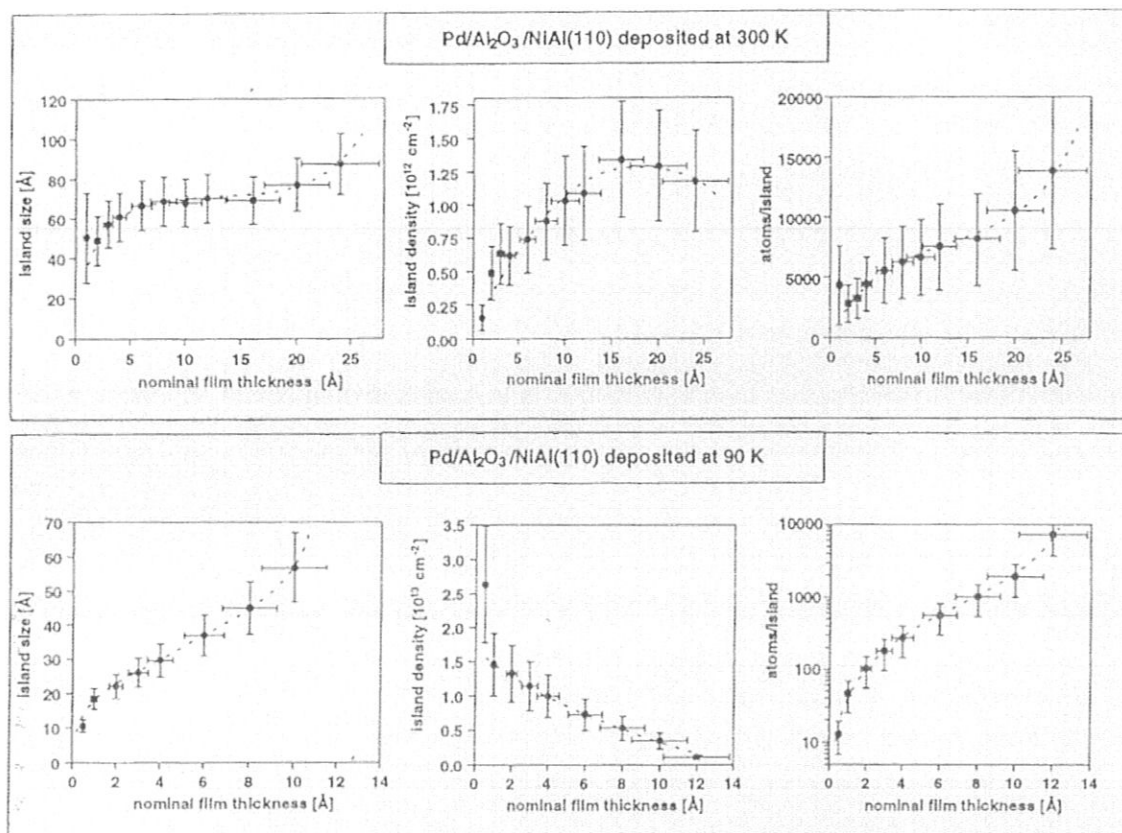
Figure 15. Dependence of several characteristic quantities for Pd growth on nominal metal coverage, as determined by LEED spot-profile analysis. Top: Average island size, island density and average number of Pd atoms per island for growth at 300 K. Bottom: Corresponding quantities for growth at 90 K.

We have investigated several different metal deposits along these lines. As pointed out above, Rh shows a similar growth mode as Pd except that it exhibits a strong tendency for nucleation at particular defects, namely at the antiphase domain boundaries of the oxide film (see Fig. 12) [133]. In Fig. 16 a LEED spot profile is plotted for a Rh deposit [113], showing the anisotropic distribution of the intensity in the shoulder as a function of direction within the Brillouin zone. The intensity maxima point in the two domain directions in line with the alignment of the antiphase domain boundaries which are decorated by the deposited metal.

A comparison of the reflex profiles found for the various metal deposits, as shown in Fig. 17, allows us to summarize the various growth modes [113]: Characteristic for Ag is the formation of rather large aggregates nucleating at the steps of the alumina film, leading to a profile where the central reflex and the shoulder are hardly discernible. Even at 90 K, the large diffusion length of Ag leads to large islands, and we note that this behaviour is very similar to the one observed for Ag on bulk single crystal surfaces [139]. The other extreme case is realized for Pt deposits: A very pronounced shoulder is observed at 90 K as well as at 300 K due to the strong interaction between metal and support leading to very small islands. Pd and Rh are intermediate cases with
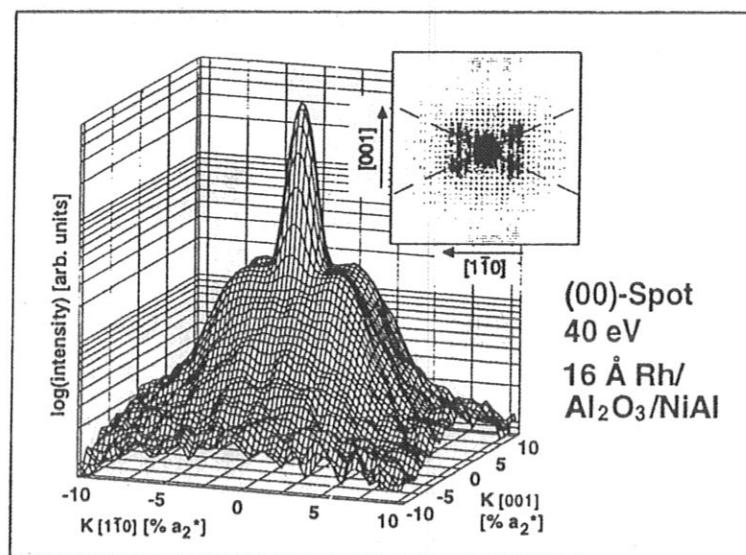
Figure 16. Two-dimensional intensity profile of the LEED (00)-spot for Al₂O₃/NiAl(110) after deposition of 16 Å Rh at 300 K. The orientation of the lattice vectors of both oxide domains is indicated in the inset.

Rh interacting slightly stronger with the substrate than Pd. In both cases, changes in the reflex profiles are observed as a function of temperature. With this comparison, we are in a position to order the metals with respect to their interaction with the substrate:
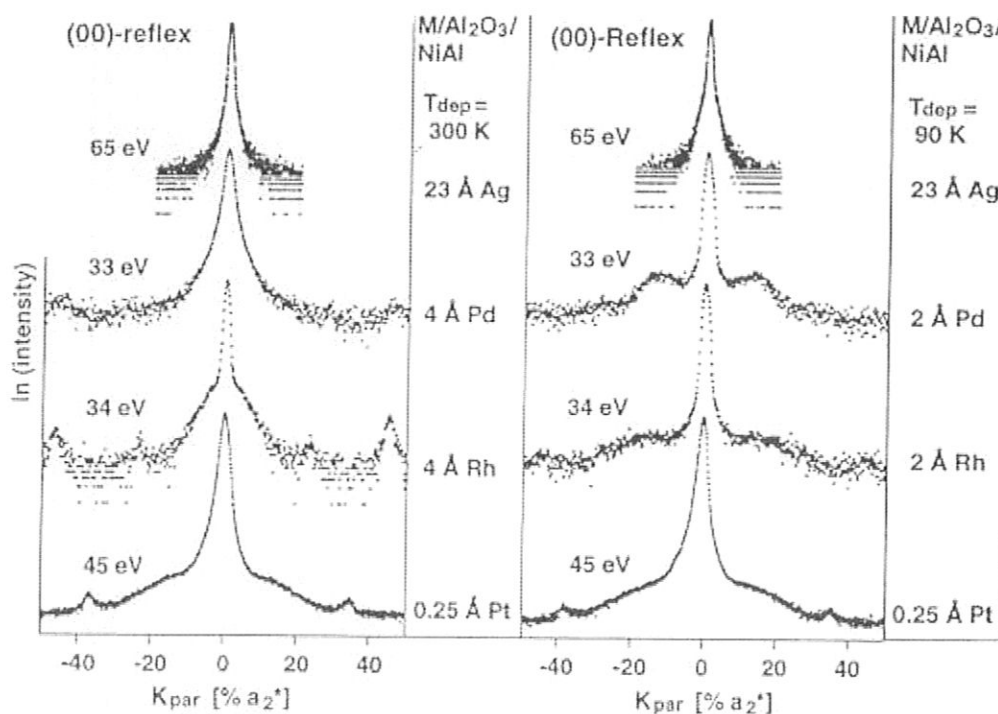
$$Pt > Rh \geq Pd > Ag.$$

Figure 17. Comparison of characteristic intensity profiles of the (00)-LEED reflex for Ag, Pd, Rh and Pt growth on Al₂O₃/NiAl(110), each at 90 and 300 K.

TABLE 1.

Enthalpies of formation of oxides [140]

ΔH^0_f	Oxide
-12.1 kJ/mol	AgO
-85.4 kJ/mol	
-90.1 kJ/mol	
-172.0 kJ/mol	PtO_2

As alluded to above, it is very difficult to explain this observation on the basis of microscopic considerations. However, a hint for the observed order may be deduced from the comparison of enthalpies of formation of the corresponding transition metal oxides. They are given in Table 1, and it is clear by inspection that the enthalpies of formation increase in the same sequence as the apparent interaction strengths observed via the present morphological studies. In other words, it might be the affinity towards oxygen that dominates the interaction. Nevertheless, we would like to stress that this is pure speculation at this point.

It has been shown above how the morphology of the transition metal deposits varies as a function of interaction strength with the substrate. This was demonstrated by changing the metal deposited. Another possibility to vary the strength of interaction is to modify the surface chemistry of the substrate. We are only at the beginning of such studies but we would like to briefly mention some results. After hydroxylation of the film - applying the procedure discussed above -, the interaction with Rh for example, deposited at 300 K, changes considerably. In particular, photoelectron spectroscopy of the Al 2p and O 1s emissions indicates characteristic changes, which are interpreted via specific interactions between the deposited metal and the hydroxylated areas on the surface [113]. Through the relatively strong interaction between Rh and the surface hydroxyl groups, a highly dispersed Rh film is formed whose morphology is more similar to the film deposited on the clean alumina film at 90 K. Of course, the change in morphology is a consequence of the changes in the interaction between Rh and the modified substrate, and this in turn shows up in variations of the electronic structure. We come back to this in connection with the study of CO adsorption on such deposits.

At this point, we have an idea of the morphology of the metal deposits. Next, electronic structure as revealed via photoelectron spectroscopy should be discussed. Figure 18 collects some Pd 3d spectra of deposits with different average island size [119-121].
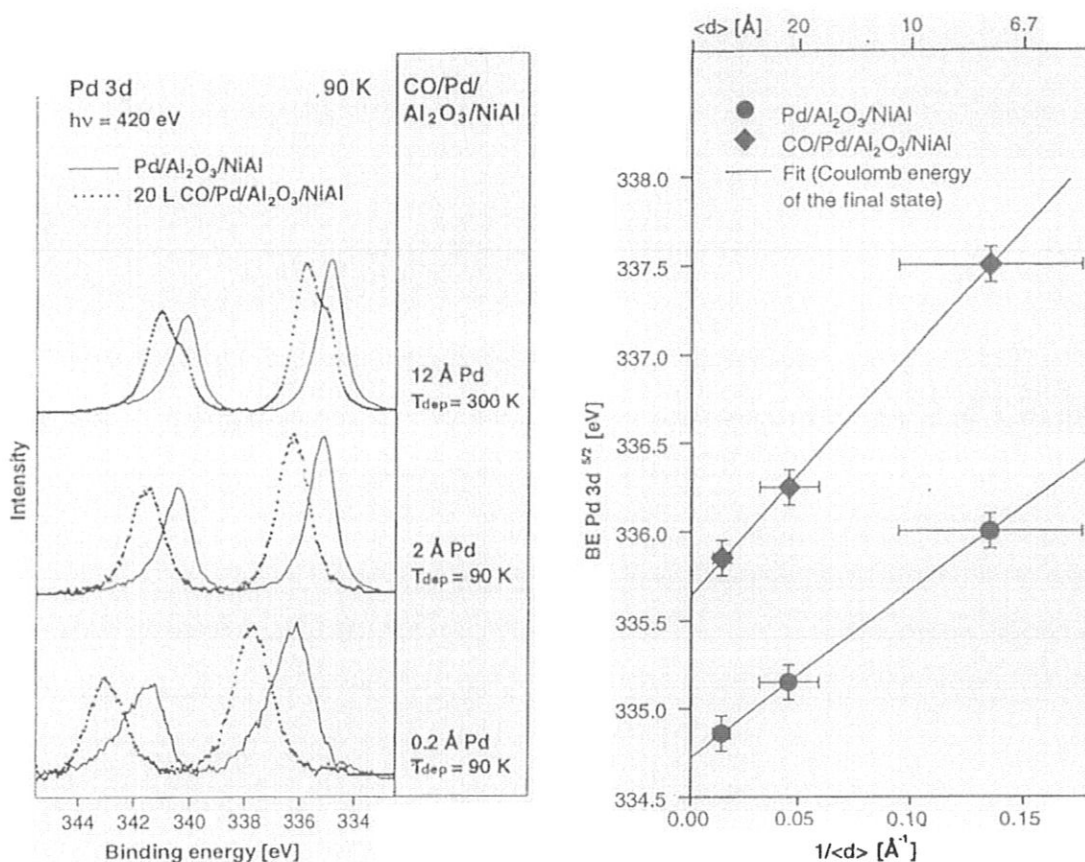
Figure 18. Left: Pd 3d core level photoelectron spectra for various Pd deposits on Al₂O₃/NiAl(110) before and after CO saturation. Right: Dependence of the binding energy of the Pd 3d surface component on reciprocal particle size for the clean and CO saturated metal films.

Two main effects are observed: Firstly, a shift to lower binding energy with increasing island size and, secondly and simultanously, a strong decrease in line widths is found. There may be several contributions to these effects, such as charge transfer, as an example for initial state effects, as well as final state effects [141-143]. An analysis of the line widths turns out to be particularly difficult [141, 142, 144-147]. At this time, we can only speculate that the inequivalence of different atoms within the aggregate combined with final state effects are the main contributions. In contrast to this, the interpretation of the binding energy shifts is more straightforward in the sense that it is possible to isolate final state contributions [143, 148]: The screening of the final state ionic charge by the valence electrons of the metal aggregate yields very characteristic binding energy shifts. While the positive charge is completely delocalized within a surface of a volume crystal, the delocalization is limited within a metal island insulated from the metallic substrate. In such a case the charge distribution depends on the mean radius of the island according to:

$$E_b \sim R^{-1} \tag{2}$$

and thus shifts the binding energy to larger values for decreasing island radii. There are several experimental observations that are in line with such an interpretation [141-144]. One is shown in Fig. 18, where the observed binding energies are plotted versus the inverse radius with perfect scaling. Therefore, we conclude that final state effects dominate the shift. If charge transfer processes in the initial state would dominate, we would expect rather strong deviations from the 1/R dependence. In addition, we would expect chemical shifts of the support levels which, however, are rather small. The existing effects can be interpreted as weak band bending effects and are of the order of 10% of the binding energy shift. The conclusion reached above, as to the dominance of final state effects connected with electrical insulation of the metal islands on the support, can be substantiated through another interesting observation. If the final state shifts were not caused exclusively by the electrons of the metal island, but also by electrons tunnelling through the thin alumina film from the metallic substrate, the final screened state would be more stable compared to the situation where screening is provided by the metal island electrons alone due to the higher degree of delocalization in the former case. Therefore, the spectroscopy of the core hole decay allows us to investigate this question further [123]. However, we shall postpone this discussion to a later point in this paper, because it is advantageous to use the decay spectra of CO adsorbed onto the metal islands to study this question in more detail.

The spectroscopy of valence electrons has also been carried out for a variety of deposited metals [113]. Without going into the details at this point, we state that for low temperature deposition of metals a Fermi edge develops at a considerably higher metal coverage as compared to the room temperature preparations. The reason, of course, is the formation of larger aggregates at room temperature due to the larger diffusion coefficient. Moreover, for the larger aggregates the development of a band structure can be observed in angle resolved photoemission experiments. The formation of a band structure shows up as a dispersion of the metal levels. Quantum size effects expressing themselves as discrete level structures have so far not been observed [113].

5. Reactivity of Oxide-Supported Metals

The appropriate starting point to discuss reactivity of oxide supported metals is a detailed analysis of the adsorption characteristics of small molecules, as for example CO, for which detailed knowledge from investigations on compact metal surfaces exists [149-152]. In photoelectron spectroscopy, the binding energy shifts as well as the line shapes of the Pd 3d ionizations change considerably upon adsorption of CO as shown in Fig. 18. The spectrum after saturation exposure of CO onto the largest Pd islands (average diameter 70 Å) at 90 K is very similar to the spectrum encountered for saturation coverage of the Pd(111) metal surface [153-155]. The Pd 3d signal of the clean Pd(111) surface contains a surface and a volume component which are shifted with
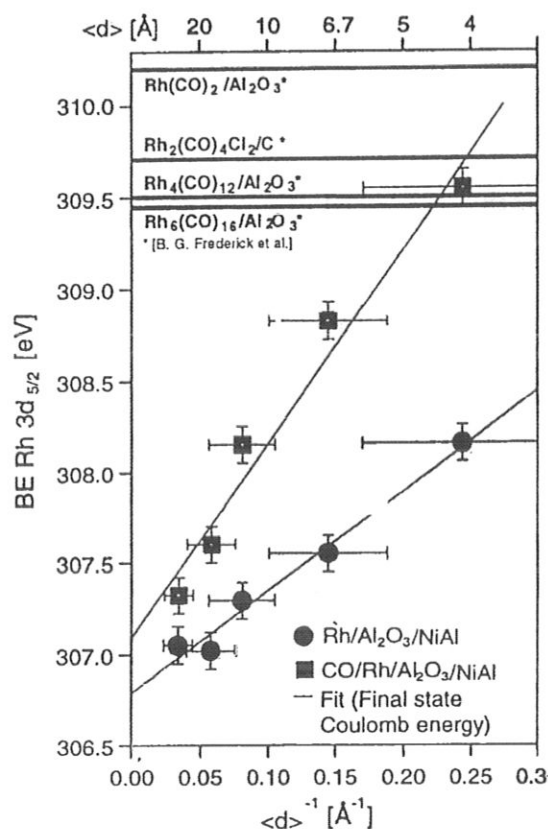
Figure 19. Particle size dependence of Rh 3d binding energies for clean and CO saturated Rh films.

respect to each other by the surface chemical shift of -0.3 eV [153]. This shift is below the present resolution. CO adsorption leads to a shift of the surface component by about 1.1 eV towards higher binding energy allowing us to separate volume and surface contributions after adsorption. The volume contribution amounts to 40% in this case, decreases to 13% for an average island size of 22 Å (2 Å, 90 K) and is below detection limit (by deconvolution of the spectra) for an average island size of 7.5 Å (0.2 Å, 90 K). Also, the CO induced binding energy shift of the Pd 3d levels increases with decreasing island size to 1.5 eV. We know from investigations of single crystal surfaces that the observed binding energy shifts depend on the number of coordinated CO molecules. A detailed analysis of the present data, together with thermal desorption data, led us to the supposition that for smaller aggregates the number of CO molecules coordinated towards a Pd metal atom increases from one to two [113]. Of course, the number of CO molecules coordinated towards a metal atom in carbonyl compounds is never reached. Nevertheless, in those cases where it is possible to compare metal ionizations in carbonyl compounds with those of deposited metal aggregates, the observed metal ionization energies in carbonyl compounds are consistent with those of the smallest deposited aggregates [156]. For Rh ionizations, Fig. 19 shows a comparison. The binding energies determined for the smallest aggregates,
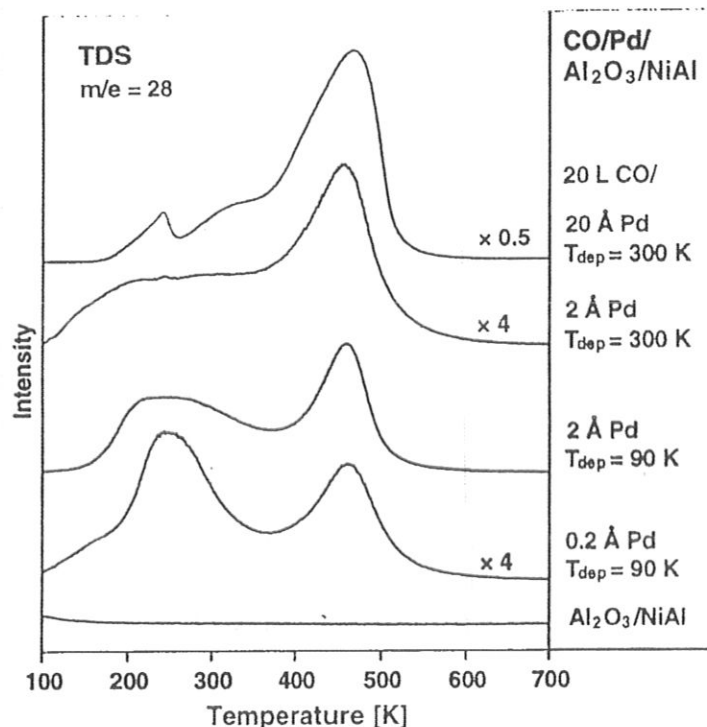
Figure 20. Thermal desorption spectra of CO adsorbed on Pd/Al₂O₃/NiAl(110) (CO exposure at 90 K, heating rate ~1.5 Ks⁻¹). The desorption spectra shown in the plot are arranged in order of decreasing average particle sizes from top to bottom.

indeed, are compatible with those measured for polynuclear metal carbonyls [156]. Only the Rh(CO)₂ species adsorbed on alumina surfaces exhibits with 310.2 eV an even higher binding energy [156]. Due to the different substrates in those cases, the comparison has to be taken with care. In general, the observed shifts scale according to a 1/R dependence similar to the clean aggregates. The different shape results from the effectively reduced number of electrons within the metal particle. Those electrons are involved in the CO-metal bond and are not available for screening.

Further information about the electronic structure of the CO adsorbate systems is of course gained via C 1s ionizations of adsorbed CO as well as via the study of valence ionizations. In addition, thermal desorption spectroscopy is very useful. Before we further analyse the photoelectron spectra, we consider the TD spectra.

In Fig. 20 several CO TD spectra of various Pd deposits are compared [121]. As expected for large Pd deposits, we find a TD spectrum similar to the one known from the single crystal surface [157]. The small, relatively sharp feature at 240 K desorption temperature is due to hydrogen contamination of the material [113]. With decreasing size of the deposited islands, a desorption maximum between 250 K and 300 K appears. Rearrangement of the metal deposit during the heating cycles is less important as revealed by a corresponding experiment, where a CO saturated deposit has been warmed to 300 K, followed by another CO saturation cycle at 90 K and a second TD
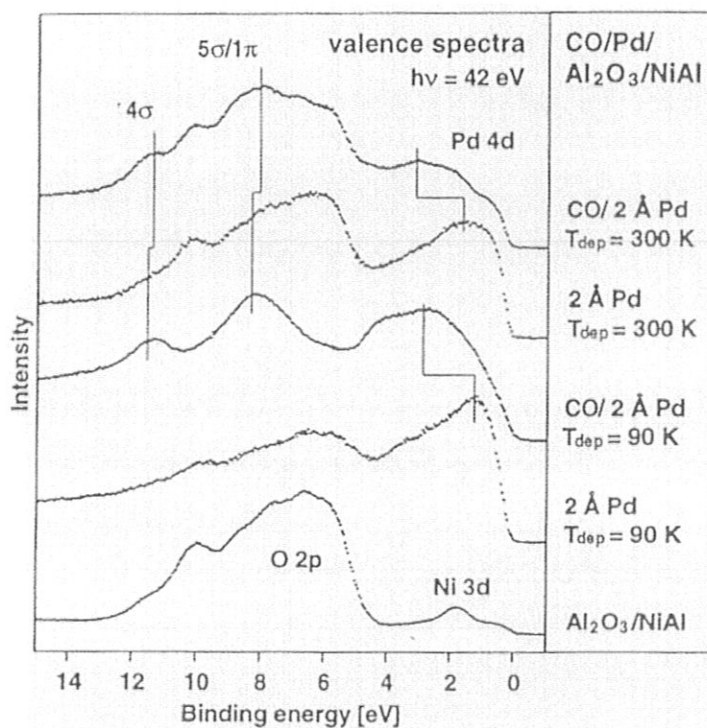
Figure 21. Comparison of valence photoemission spectra for clean and CO saturated Pd deposits on Al₂O₃/NiAl(110) grown at 300 and 90 K.

experiment. The second TD spectrum is almost identical to the first one, indicating that the desorption at lower temperature, i.e. between 250 K and 300 K, is an inherent property of small Pd deposits.

We now turn back to the electronic properties as revealed by photoemission. Figure 21 gives an impression of the changes induced by CO adsorption in the valence photoelectron spectra of the metal deposits [121]. We recognize at 11 eV and 8 eV binding energies the CO 4σ and CO $5\sigma/1\pi$ emissions, respectively. The considerably higher intensity of the adsorbate induced features for the deposit at 90 K as compared with the 300 K deposit may be interpreted - on the basis of the growth behaviour - as a larger surface contribution in the former case [113]. Also, considerable changes are induced in the region of the Pd 4d emissions. The size dependent effects are clearly apparent. Due to the small volume contribution for the low temperature deposition, CO adsorption leads to much larger changes near the Fermi energy for the 90 K deposit. A more detailed analysis has to await further experiments.

The C 1s spectra of the CO adsorbates are shown in Fig. 22 and are typical for molecular CO. Therefore, it is appropriate to compare the spectra of the metal deposits with those of carbonyl compounds [158-160] on one hand and with an adsorbate on a Pd(111) surface [161] on the other hand again. The weak fine structure of the surface adsorbate may be traced back to the co-existence of several adsorption sites. The C 1s spectrum taken for large Pd deposits is very similar to the adsorbate on the extended
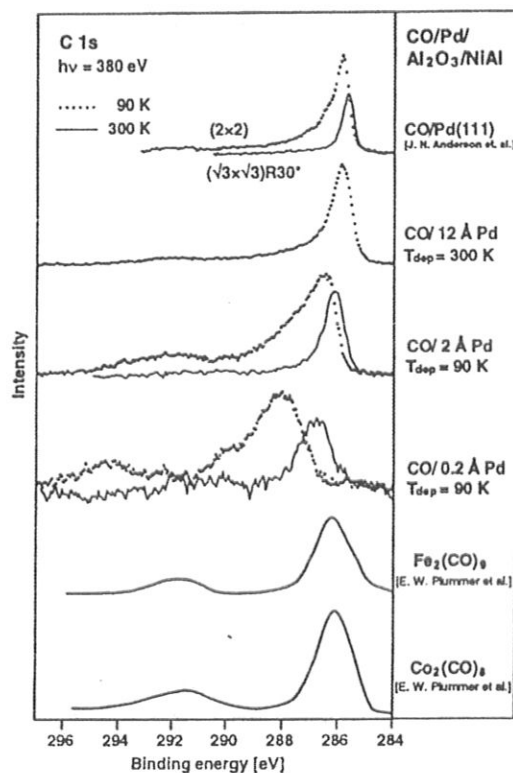
Figure 22. C 1s core level photoelectron spectra for CO/Pd/Al$_2$O$_3$/NiAl(110) after CO saturation at 90 K and after heating to 300 K. Additionally, C 1s spectra of two ordered CO superstrutures on Pd(111) as well as spectra of two transition metal carbonyls are shown for comparison.

surface. As we turn to smaller metal islands, we find shifts to higher binding energies, increase of line width and the occurrence of an intense, so called shake-up satellite structure [159, 162-168]. After desorption of the weakly adsorbed CO by heating to 300 K, we find a shift to lower binding energies, decrease of line widths as well as asymmetry and shake-up satellite intensity. Shake-up satellites are a consequence of the complex many particle processes occurring during photoemission and have been discussed in the literature quite extensively [159, 162-168]. The satellites are due to the population of various ion states in the ionization process. The intensity in the spectrum strongly depends on the CO-metal bonding [158, 159, 168]. A detailed analysis shows that charge transfer satellites gain relatively large intensities if the CO-metal coupling is weak. This means that, in agreement with the TDS experiments, the change in the satellite intensities is indicative of a considerable change of the electronic structure as a function of aggregate size: While the strength of the chemisorption bond for small aggregates is sensitive to coverage, this is to a much lesser extent true for larger aggregates and single crystal surfaces. Due to the lower degree of ordering in the smaller aggregates, we have to expect a wider distribution of adsorption geometries and we believe that this fact contributes to the observed larger line widths. However, other contributions are expected [166, 169-171] but will not be discussed here. The observed
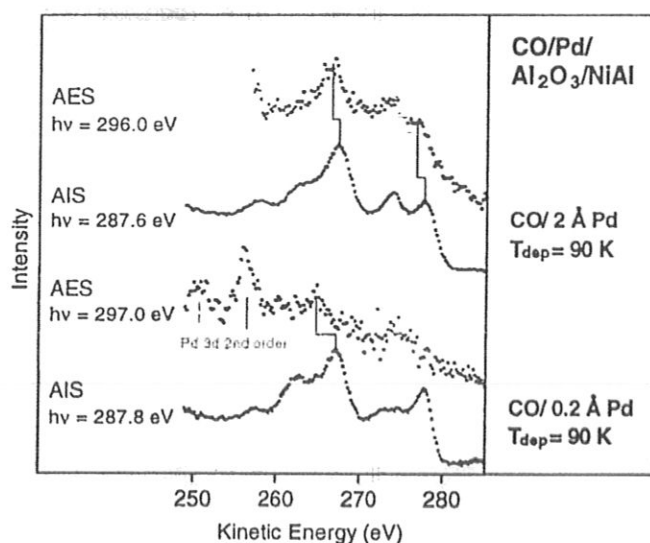
Figure 23. Comparison of autoionisation and Auger spectra for CO/Pd/Al₂O₃/NiAl(110).

shifts of the binding energies are, as discussed for the Pd ionizations, mainly caused by final state effects, i.e. screening via charge transfer from the metal aggregates [142]. As announced above, we may use the CO core hole decay spectra to show that the screening charge only flows from the metal island and not from the metal substrate underneath the alumina film. Since a state with a core hole is highly unstable, it will rapidly decay for example by electron emission. By comparing the decay of the neutral core excited state, i.e. autoionization (AI) [172, 173] spectrum, with that of the core ionized state (the Auger electron (AE) spectrum) as shown in Fig. 23, the screening dynamics occurring within the core hole lifetime (typically 10^{-15} s) can be studied [123]. For a free CO molecule for example, the two hole (2h) states in the AE spectrum are shifted towards lower kinetic energies relative to the two hole one particle (2h-1p) states (spectator peaks) in the AI spectrum due to the absence of screening from the spectator electron in the $2\pi^*$ orbital. Thus, the AI and AE spectra are fundamentally different. For CO chemisorbed on a metal, on the other hand, the strong coupling of the $2\pi^*$ orbital with the metal states quenches this difference, leading to AI and AE spectra which are nearly identical. Comparing the AE and AI spectra of the small particles obtained at 90 K, we indeed find a "spectator shift" which increases as the particle size decreases. This shows that there is also no detectable charge transfer to the clusters occurring during the core hole lifetime.

In contrast to the photoemission experiments, which are dominated by final state effects, the x-ray absorption spectra are much less influenced by such effects as revealed by the spectra shown in Fig. 24 [113]. We consider the excitation of a C 1s or O 1s electron into the antibonding $2\pi^*$ orbital of CO [174-178]. Since the $2\pi^*$ electron remains on the molecule, the $2\pi^*$ electron itself screens the core hole. Therefore, while
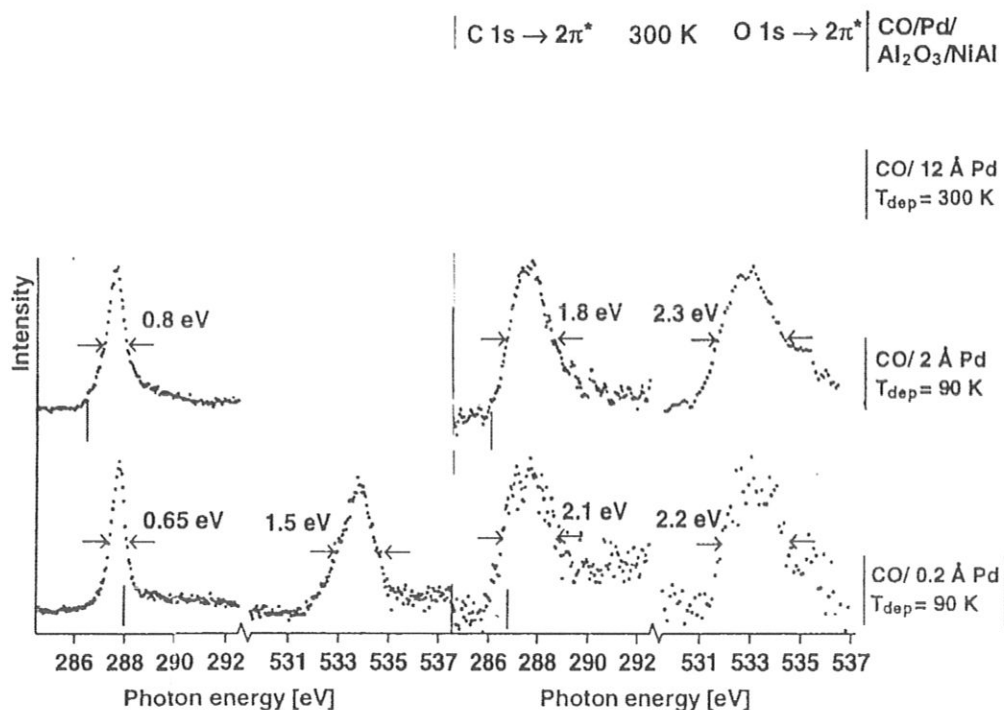
Figure 24. X-ray absorption spectra of the C 1s and O 1s → 2π* resonances for CO/Pd/Al$_2$O$_x$/NiAl(110). Left: After CO saturation at 90 K. Right: After heating to 300 K. The corresponding XPS binding energies relative to the fermi level of the NiAl substrate are marked with lines.

in the case of the core ionization the binding energy shift is strongly depending on screening, mainly provided by the electrons of the metal aggregate and thus on particle size, the x-ray absorption signal depends much less on these parameters. However, the signal is strongly influenced by the strength of the CO-metal bond as the following argument illustrates: The synergetic σ-donor-π-acceptor bonding mechanism leads to a strong interaction between CO-π-orbitals and occupied Pd-4d-orbitals. Since the 4d orbitals form a band, the interaction with the CO-2π orbitals lead to a CO-2π* density of states distribution whose width depends on the CO-metal interaction. Systematic investigations of adsorbates on single crystal surfaces have shown that life time of the excitation, vibrational excitation and intermolecular interaction play a less significant role for the x-ray absorption spectra [178]. Two effects dominate: Firstly, the width of the resonance increases with increasing chemisorption bond strength while the morphology does not change, and, secondly, it also increases with increasing coordination of the CO molecule, i.e. when the CO molecule changes site from a top to bridge to hollow site. These results may now be used to interpret the spectral changes observed in Fig. 24. While the ionization potential, indicated by the bar in the C 1s x-ray absorption spectra, shifts to larger values with decreasing aggregate size, the 2π* resonance stays constant in energy. Simultaneously, the resonance becomes narrower as expected for decreasing chemisorption energy. The same is true for the O 1s → 2π* resonance. After heating the sample from 90 K to 300 K the resonances become wider,

in full agreement with the above discussion. Therefore, it is quite clear that also the x-ray absorption spectra indicate a stronger CO-metal bond for smaller CO coverage.

In fact, all applied experimental methods point for the Pd/Al$_2$O$_3$ system in the regime of low CO coverage towards a strong CO-metal bond for all island sizes. For small island sizes, however, the CO bond strength decreases considerably with increasing CO coverage, and it is for the smallest aggregates only situated in the range of a weak chemisorptive bond. It is now rather interesting to compare the results for the Pd/Al$_2$O$_3$ system with those for the Rh/Al$_2$O$_3$ system. Both, TDS as well as x-ray absorption indicate in this case that the CO adsorption properties are much less sensitive to the size of the aggregates. Only the smallest aggregates show a very weak dependence. A possible explanation involves different CO adsorption geometries on the smallest aggregates, because it is well known that Rh tends to form geminal dicarbonyl species [156]. This is also in agreement with investigations [179-182] according to which Rh restructures upon CO adsorption at 300 K which leads to higher adsorption capacities at 90 K. We have followed these processes by a LEED profile analysis coupled with TDS experiments [113].

For Rh deposits, we find a new reaction channel which is not observed in our experiments for the case of Pd deposits [29, 183-186]. Upon heating, the CO adsorbates on the Rh deposits, CO dissociation is experimentally observed. This reaction channel is activated between 300 K and 400 K and can be followed via the C 1s photoelectron spectra as shown in Fig. 25. The carbidic carbon signal due to the presence of atomic carbon on the Rh deposits appears at 284 eV binding energy upon heating. After completing the reaction, only atomic carbon remains, while the molecular signal has completely disappeared. X-ray absorption assures that the CO-2π* resonance has also disappeared [113]. The present Rh model systems, therefore, allow us to study CO dissociation as a function of the size of the aggregates [184-186]. A corresponding series of spectra where systems with different average aggregate sizes were subjected to the reaction are shown in Fig. 25b. The signals recorded at 90 K after CO saturation are compared with those after heating to 400 K and 600 K, respectively. If we consider the ratio of molecular CO intensity with respect to atomic carbon intensity for small aggregates versus larger aggregates, we realize that this ratio decreases as the aggregate size increases. A more detailed analysis [113] of the data also corroborates the conclusion that the smallest aggregates, indeed, exhibit the smallest dissociation activity [184-186]. Several factors contribute to this. One, of course, must be connected with the variation of the electronic structure of the aggregate as a function of the size. However, there are other effects, one of which may be a simple geometric one. The products of the dissociation process, atomic carbon and oxygen, prefer to adsorb in coordination sites of high symmetry. Calculations [187] predict that those sites have to be at a minimal separation. Therefore, the dissociation channel can only be operative if the aggregate has a particular minimal size. Such a process is schematically represented in Fig. 25c.
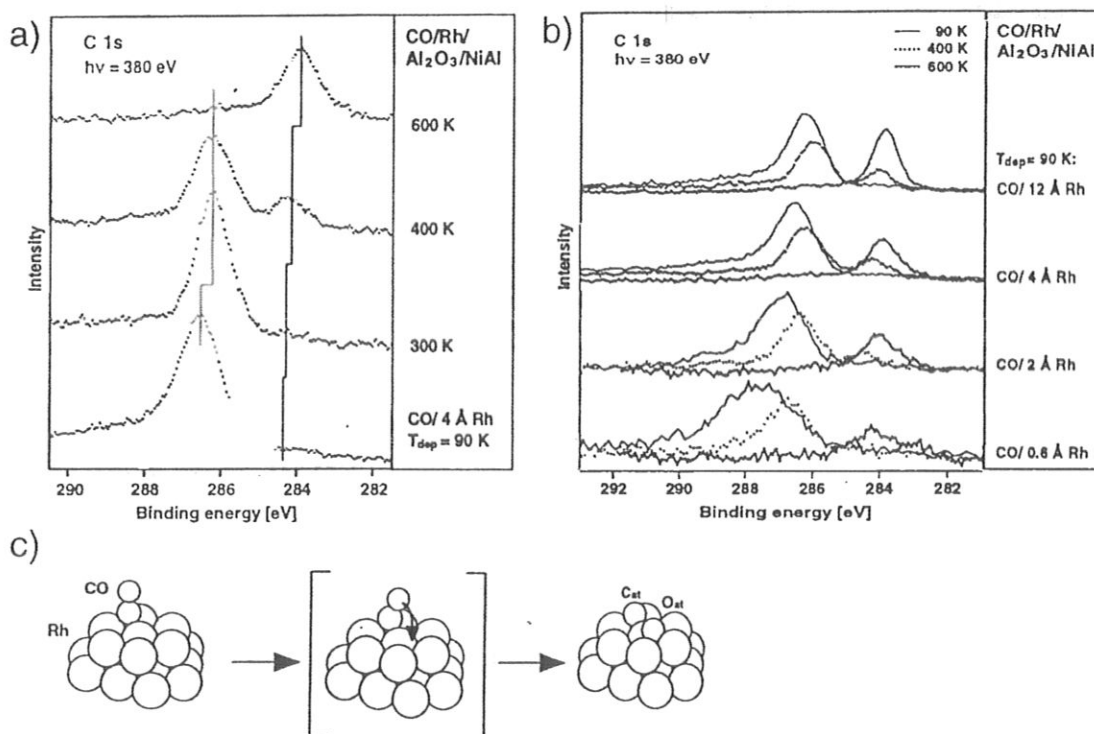
Figure 25. a) Series of C 1s core level photoelectron spectra for Rh/Al₂O₃/NiAl(110) after CO saturation at 90 K and after heating to the temperatures given in the plot.
b) Comparison of the normalized C 1s photoelectron spectra for various nominal Rh coverages after CO saturation at 90 K and after heating to 400 and 600 K. c) Schematic representation of the CO dissoziation process.

We have reached a point where we may correlate chemical reactivity with the size of the deposited aggregates. If we want to understand effects which occur in connection with catalyst preparation, we must try to influence the morphology of the metal deposit by chemical modification and study its consequences for the adsorption and reaction properties [179-182]. While we have already studied chemical modification of the alumina substrate on the morphology of the metal deposit, we now investigate the consequences on CO adsorption. As discussed above, there were indications that the Rh substrate interaction is strongly influenced if the alumina substrate was hydroxylated [188-193]. The main observation was that while on the clean substrate Rh deposits restructure under CO exposure, this is inhibited upon hydroxylation. We have followed the restructuring via CO adsorption at 300 K. In contrast to the non modified substrate where the restructuring shows up in a higher adsorption capacity upon reexposure at low temperature, this effect is not observed on the chemically modified substrate. A strong interaction between metal and support is compatible with these findings. If we finally consider the dissociation activities in the chemically modified system, we find a reduction by about a factor of two with respect to the non modified system. We can trace this back to the formation of smaller Rh aggregates on the hydroxylated substrate, which exhibit, as pointed out above, a reduced dissociation activity. Summarizing at this point, we may state that investigations on model systems
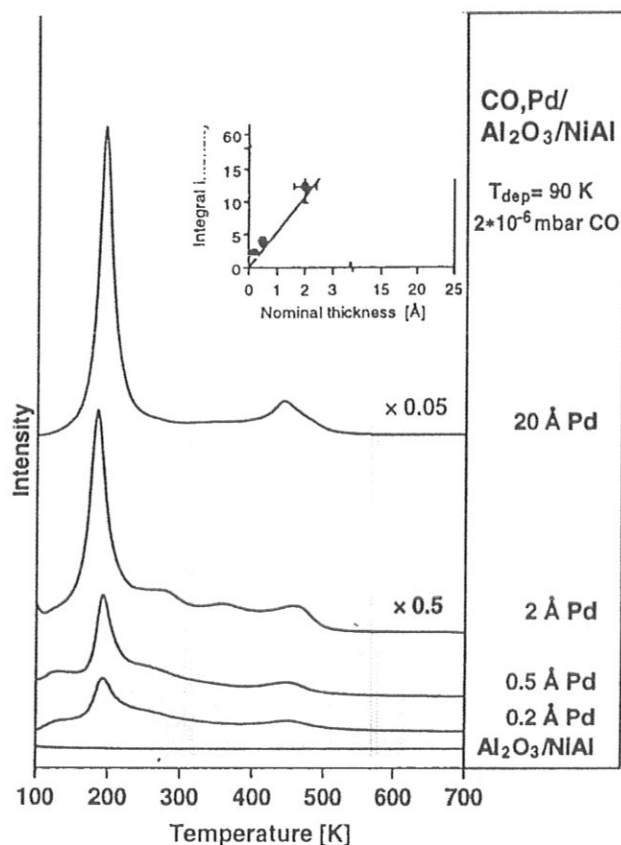
Figure 26. Thermal desorption spectra for various nominal Pd coverages on Al₂O₃/NiAl(110), deposited at 90 K in CO atmosphere (heating rate ~1.5 Ks⁻¹).
The dependence of the integral desorption intensity on nominal metal coverage is shown in the inset.

allow to a certain degree the simulation of typical situations encountered in connection with real catalyst preparation. Our results are in line with the well-documented CO induced Rh redispersion on Al_2O_3 [179-182] and other substrates [194-196]. In these investigations, it was shown that at high enough CO partial pressures a redispersion occurs, accompanied by the formation of geminal rhodium-dicarbonyl species. There are indications that in real systems the dicarbonyl formation also involves hydroxyls on the surface. Further investigations on the model systems, in particular infra-red investigations, have to be carried out.

Another option for chemical modification is to deposit the metal in the presence of a gas atmosphere. Under these circumstances, the adsorbate influences the growth process as a „surfactant" [197-200]. As an example, we have studied the deposition of Pd aggregates in a CO atmosphere [118]. Figure 26 shows TD spectra after deposition of various amounts of metal. The spectra are dominated by a relatively sharp signal at 200 K maximum desorption temperature typical for decomposition of a compound. The weak signals up to 500 K are due to desorption processes from fragments and agglomerates formed via decomposition. The intensity of the compound decomposition is
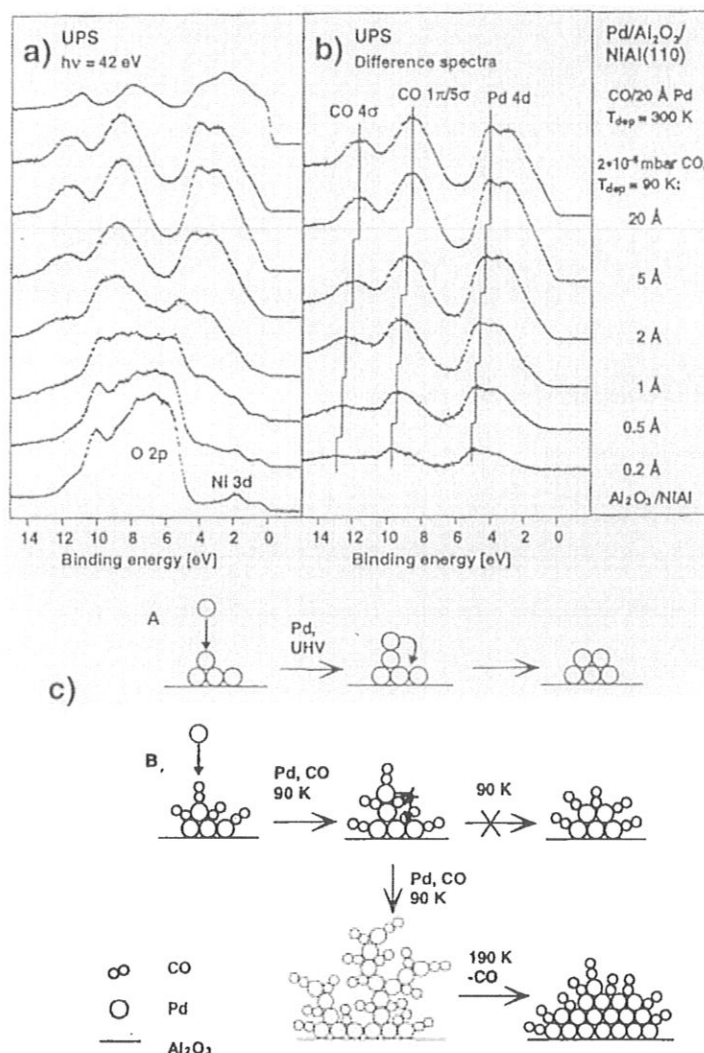
Figure 27. a) Valence photoelectron spectra for successive deposition of Pd in CO atmosphere. A valence spectrum for deposition of 20 Å Pd at 300 K in UHV after CO saturation is shown for comparison.
b) Difference spectra after subtraction of oxide- and substrate-induced emission.
c) Schematic representation of a possible growth model for Pd deposition in CO atmosphere.

directly proportional to the deposited amount of metal as indicated in the inset in Fig. 26. The valence photoelectron spectra as well as the core hole spectra support the claim that a transition metal carbonyl compound is formed [149, 158, 159]. Figure 27 shows spectra of the valence region, that were obtained after stepwise Pd deposition. By calculating the difference spectra, we can suppress the substrate emssion as also shown in Fig. 27. It becomes obvious that, except for a slight shift in binding energy, the spectra show little change over the whole coverage range. The spectra are dominated by the $5\sigma/1\pi$ emission at 8.8 eV and the 4σ emission at 11.9 eV [149, 201] as well as the ligand field splited Pd 4d signals [158, 202] at 4.1 eV and 3.3 eV for a Pd coverage equivalent to 20 Å. With decreasing coverage, the signals shift to lower binding energy by about 1 eV. An interesting observation may be made in the range of the Fermi

energy. Even for the highest coverages the density of states in this energy range remains negligable. In agreement with the proposed formation of a compound, we can exclude the formation of large metallic aggregates. Schematically, the growth of the carbonyl compound may be represented as illustrated in Fig. 27c. This model of the formation of fractal, low dimensional structures takes account of the various observations by LEED, XPS and TDS. The formation of such species is quite unexpected because binary Pd carbonyl species in general exhibit rather low stabilities [203-209]. In contrast to a similar study for Pt deposition on TiO_2 [14], where the CO induced changes have been dicussed on a thermodynamic basis, kinetic mechanisms must be active in the present case.

6. Synopsis

It is possible to prepare oxide surfaces with different crystallographic orientations by applying techniques of epitaxial growth. The systems are well structured and allow a variety of spectroscopic investigations. Adsorption of molecules may be studied and some interesting conclusions with respect to catalytically relevant reactions on the oxide surfaces may be drawn. Most relevant, however, the epitaxial oxide films can be used as support materials for the deposition of metals. The morphology and growth modes of various transition metals have been studied on a model alumina surface. These studies also include chemical modification of the substrate and the investigation of the consequences for the growth of metals. Adsorption and reactivity of small molecules have been investigated with a variety of techniques. We have identified CO dissociation as a size dependent process in the case of small Rh aggregates. The influence of chemical modification of the substrate onto such processes has also been considered. Deposition of metals within an adsorbate atmosphere is an interesting option to prepare otherwise hardly accessible systems.

In summary, studies on model systems will continue to allow us to gain interesting insight into processes relevant in the preparation and function of catalysts.

7. Acknowledgements

8. References

1. A.B. Stiles (ed., 1987) *Catalyst Supports and Supported Catalysts*, Butterworth, Boston.
2. B.C. Gates, L. Guczi and H. Knözinger (eds., 1986) *Metal Clusters in Catalysis*, *Studies in Surface Science and Catalysis*, Vol. 29, Elsevier, Amsterdam.
3. H.-J. Freund *Angew. Chemie*, submitted.
4. G.A. Somorjai and J. Carraza (1986) *Ind. Eng. Chem. Fundam.* 25, 63.
5. H.-J. Freund and E. Umbach (eds., 1993) *Adsorption on Ordered Surfaces of Ionic Solids and Thin Films*, Springer Series in Surface Sciences, Vol. 33, Springer Verlag, Heidelberg.
6. C. Noguera (1996) *Physics and Chemistry at Oxide Surfaces*, Cambridge Univ. Press, Cambridge.
7. V.E. Henrich and P.A. Cox (1994) *The Surface Science of Metal Oxides*, Cambridge Univ. Press, Cambridge.
8. H.-J. Freund (1995) *Ber. Bunsenges. Phys. Chemie* 99, 1261.
9. H.-J. Freund (1995) *Phys. Stat. Sol (b)* 192, 407.
10. H.-J. Freund (1996) Nato Advanced Study Institute NATO ASI Series C, Vol. 232, Kluwer Acad. Press, p. 474.
11. S.K. Purnell, X. Xu, D.W. Goodman and B.C. Gates (1994) *Langmuir* 10, 3057; (1994) *J. Phys. Chem.* 98, 4076.
12. M.C. Wu, W.S. Oh and D.W. Goodman (1995) *Surf. Sci.* 330, 61.
13. D.W. Goodman (1995) *Chem. Rev.* 95, 523; (1995) *Surf. Rev. and Lett.* 2, 9.
14. H.-P. Steinrück, F. Pesty, L. Zhang and T.E. Madey (1995) *Phys. Rev. B* 51, 2427.
15. M.C. Wu and P.J. Møller (1989) *Surf. Sci.* 221, 250.
16. P.J. Møller and M.C. Wu (1989) *Surf. Sci.* 224, 265.
17. M.C. Wu and P.J. Møller (1990) *Surf. Sci.* 235, 228.
18. M.C. Wu and P.J. Møller (1991) in S.Y. Tong, M.A. van Hove, K. Takayanaki and X.D. Xider (eds.), *The Structure of Surfaces III* , Springer Verlag, Berlin, p. 652.
19. M.C. Wu and P.J. Møller (1990) *Surf. Sci.* 250, 179.
20. Q. Guo and P. J. Møller (1990) *Vacuum* 41, 1114.
21. P.J. Møller and Q. Guo (1991) *Thin Sol. Films* 201, 267.
22. P.J. Møller and J. Nerlov (1993) *Surf. Sci.* 307-309, 591.
23. O. Ge and P.J. Møller (1994) *Appl. Surf. Sci.* 82-83, 305.
24. Q. Guo and P.J. Møller, *Surf. Sci. Lett.*, in press.
25. A. Ludviksson, K.H. Ernst, R. Zhang and C.T. Campbell (1993) *J. Catal.* 141, 380.

26. K.H. Ernst, A. Ludviksson, R. Zhang, I. Yoshihara and C.T. Campbell (1993) *Phys. Rev. B* **47**, 13782.

27. E.I. Altman and R.J. Gorte (1988) *Surf. Sci.* **195**, 392; (1988) *J. Catal.* **113**, 185.

28. H. Cordatos, T. Bunluesin and R.J. Gorte (1995) *Surf. Sci.* **323**, 219.

29. E.I. Altman and R.J. Gorte (1989) *Surf. Sci.* **216**, 386.

30. J.-M. Pan, B.L. Maschhoff, U. Diebold and T.E. Madey (1993) *Surf. Sci.* **291**, 381.

31. U. Diebold, J.-M. Pan and T.E. Madey (1993) *Phys. Rev. B* **47**, 3868.

32. J.-M. Pan and T.E. Madey (1993) *J. Vac. Sci. Technol. A* **11**, 1667.

33. C. Duriez, C.R. Henry and C. Chapon (1991) *Surf. Sci.* **253**, 190.

34. C.R. Henry, C. Chapon, C. Duriez and S. Giorgio (1991) *Surf. Sci.* **253**, 177.

35. C.R. Henry, C. Chapon, C. Goyhenex and R. Monot (1992) *Surf. Sci.* **272**, 283.

36. C. Goyhenex, M. Meunier and C.R. Henry (1996) *Surf. Sci.* **350**, 103.

37. C. Goyhenex, M. Croni, C. Claeys and C.R. Henry (1996) *Surf. Sci.* **352-354**, 475.

38. P. Légaré and B.R. Bilwes (1992) *Surf. Sci.* **279**, 159.

39. P. Légaré, F. Finck, R. Roche and G. Maire (1989) *Z. Phys. D* **12**, 19.

40. E. Gillet and V. Matolin (1991) *Z. Phys. D* **19**, 361.

41. B. Ealet and E. Gillet (1993) *Surf. Sci.* **281**, 91.

42. S. Ogawa and S. Ichikawa (1995) *Phys. Rev. B* **51**, 17231.

43. J.-W. He and P.J. Møller (1986) *Chem. Phys. Lett.* **129**, 13; P.J. Møller (1994) in J. Nowotny (ed.) *Science of Ceramic Interfaces II*, p. 473.

44. T. E. Madey, U. Diebold and J.-M. Pan, (1993) in H.-J. Freund and E. Umbach (eds.) *Adsorption on Ordered Surfaces of Ionic Solids and Thin Films*, Springer Series in Surface Science, Vol. 33, Springer Verlag, Heidelberg, p. 147.

45. H. Kuhlenbeck (1994) *Appl. Phys. A* **59**, 469.

46. W. Weiss, A. Barbieri, M.A. van Hove and G.A. Somorjai (1993) *Phys. Rev. Lett.* **71**, 1848; A. Barbieri, W. Weiss, M.A. van Hove and G.A. Somorjai (1994) *Surf. Sci.* **302**, 259.

47. H. Kuhlenbeck, G. Odörfer, R. Jäger, G. Illing, M. Menges, Th. Mull, H.-J. Freund, M. Pöhlchen, V. Staemmler, S. Witzel, C. Scharfschwerdt, K. Wennemann, T. Liedtke and M. Neumann (1991) *Phys. Rev. B* **43**, 1969.

48. M. Haßel and H.-J. Freund (1995) *Surf. Sci.* **325**, 163.

49. D. Cappus, M. Haßel, E. Neuhaus, M. Heber, F. Rohr and H.-J. Freund (1995) *Surf. Sci.* **337**, 268.

50. D. Cappus, X. Xu, D. Ehrlich, B. Dillmann, C.A. Ventrice Jr., K. Al-Shamery, H. Kuhlenbeck and H.-J. Freund (1993) *Chem. Phys.* **177**, 533.

51. a.) S.M. Vesecky, X. Xu and D.W. Goodman (1994) *J. Vac. Sci. Technol. A* **12**, 2114; b) M.C. Wu, C.M. Truong and D.W. Goodman (1993) *J. Phys. Chem.* **97**, 4182; c) C.M. Truong, M.C. Wu and D.W. Goodman (1993) *J. Am. Soc.* **115**, 3647;

d) J.W. He, J.S. Corneille, C.A. Estrada, M.C. Wu and D.W. Goodman (1992) *J. Vac. Sci. Technol. A* **10**, 2248;

e) M. C. Wu, C.A. Estrada, J. S. Corneille and D.W. Goodman (1992) *J. Chem. Phys.* **96**, 3892.

52. D. Cappus, J. Klinkmann, H. Kuhlenbeck and H.-J. Freund (1995) *Surf. Sci. Lett.* **325**, L 421.

53. M. Schönnenbeck, D. Cappus, J. Klinkmann, H.-J. Freund, L.G.M. Pettersson and P.S. Bagus (1996) *Surf. Sci.* **347**, 337.

54. N. Floquet and I.C. Dufour (1983) *Surf. Sci.* **126**, 543.

55. V.E. Henrich (1976) *Surf. Sci.* **57**, 385.

56. H. Oniski, C. Egawa, T. Aruga and Y. Iwasawa (1994) *Surf. Sci.* **310**, 135.

57. C.R. Henry and H. Poppa (1990) *Thin Sol. Films* **189**, 303.

58. J.S. Foord and R.M. Lambert (1986) *Surf. Sci.* **169**, 327.

59. C.A. Ventrice Jr., H. Hannemann, A. Brodde and H. Neddermeyer (1994) *Phys. Rev. B* **49**, 5773;

    H. Hannemann, C.A. Ventrice, Th. Bertrams, A. Brodde and H. Neddermeyer (1994) *Phys. Stat. Sol. (a)* **146**, 289.

60. F. Rohr, K. Wirth, J. Libuda, D. Cappus, M. Bäumer and H.-J. Freund (1994) *Surf. Sci.* **315**, L977.

61. H. Kuhlenbeck, M. Frank, G. Lilienkamp, C. Koziol, T. Schmidt, E. Bauer and H.-J. Freund, private communications.

62. H. Kuhlenbeck, C. Xu, B. Dillmann, M. Haßel, B. Adam, D. Ehrlich, S. Wohlrab, H.-J. Freund, U.A. Dittinger, H. Neddermeyer, M. Neuber and M. Neumann (1992) *Ber. Bunsenges. Phys. Chem.* **96**, 15.

63. C.A. Ventrice, D. Ehrlich, E.L. Garfunkel, B. Dillmann, D. Heskett and H.-J. Freund (1992) *Phys. Rev. B* **46**, 12892.

64. M. Bender, D. Ehrlich, I.N. Yakovkin, F. Rohr, M. Bäumer, H. Kuhlenbeck, H.-J. Freund and V. Staemmler (1995) *J. Phys.: Condens. Matter* **7**, 5289.

65. C. Xu, M. Haßel, H. Kuhlenbeck and H.-J. Freund (1991) *Surf. Sci.* **258**, 23.

66. C. Xu, B. Dillmann, H. Kuhlenbeck and H.-J. Freund (1991) *Phys. Rev. Lett.* **67**, 3551.

67. F. Rohr, M. Bäumer, H.-J. Freund, S. Müller, L. Hammer and K. Heinz, in preparation.

68. B. Dillmann, O. Seiferth, G. Klivenyi, F. Rohr, I. Hemmerich, M. Bender, I. Yakovkin, D. Ehrlich and H.-J. Freund, *Farad. Disc. Chem. Soc.*, submitted.

69. H.-J. Freund, B. Dillmann, O. Seiferth, G. Klivenyi, M. Bender, D. Ehrlich, I. Hemmerich and D. Cappus, *Catal. Today*, in press.

70. B. Dillmann (1996) PhD-Thesis, Ruhr-Universität Bochum.

71. I. Hemmerich, F. Rohr, O. Seiferth, B. Dillmann and H.-J. Freund, *Z. Phys. Chem. NF*, submitted.

72. C. Xu (1991) PhD-Thesis, Ruhr-Universität Bochum.

73. F. Rohr, PhD-Thesis, Ruhr-Universität Bochum, in preparation.

74. H.-J. Freund, H. Kuhlenbeck and V. Staemmler (1996) *Rep. Progr. Phys.* **59**, 283.

75. U.J. Katter, H. Schlienz, M. Beckendorf and H.-J. Freund, *Ber. Bunsenges. Phys. Chem.* **97**, 340.

76. H. Schlienz, M. Beckendorf, U.J. Katter, T. Risse and H.-J. Freund (1995) *Phys. Rev. Lett.* **74**, 761.

77. Th. Risse, U.J. Katter, T. Hill, H. Hamann and H.-J. Freund, *Langmuir*, submitted.

78. R.M. Jaeger, H. Kuhlenbeck, H.-J. Freund, M. Wuttig, W. Hoffmann, R. Franchy, and H. Ibach (1991) *Surf. Sci.* **259**, 235.

79. M. Wuttig, W. Hoffmann, R. Jaeger, H. Kuhlenbeck and H.-J. Freund (1991) *Mat. Res. Soc. Symp. Proc.* **221**, 143.

80. R.M. Jaeger, K. Homann, H. Kuhlenbeck and H.-J. Freund (1993) *Chem. Phys. Lett.* **203**, 41.

81. R.M. Jaeger, J. Libuda, M. Bäumer, K. Homann, H. Kuhlenbeck and H.-J. Freund (1993) *J. Electron Spectrosc. Relat. Phenom.* **64/65**, 217.

82. J. Libuda, M. Bäumer and H.-J. Freund (1994) *J. Vac. Sci. Technol. A* **12**, 2259.

83. J. Libuda, F. Winkelmann, M. Bäumer, H.-J. Freund, Th. Bertrams, H. Neddermeyer and K. Müller (1994) *Surf. Sci.* **318**, 61.

84. M. Bender, K. Al-Shamery and H.-J. Freund (1994) *Langmuir* **10**, 3081.

85. K.P. Huber, G. Herzberg (1979) *Molecular Spectra and Molecular Structure, IV: Constants of Diatomic Molecules*, Van Nostrand, New York.

86. P.W. Tasker (1979) *J. Phys. C: Solid State Phys.* **12**, 4977.

87. J.W. Tasker (1979) *Phil. Mag. A* **39**, 119.

88. R. Lacmann (1965) *Colloq. Int. CNRS* **152**, 195.

89. D. Wolf (1992) *Phys. Rev. Lett.* **68**, 3315.

90. K. Refson, R.A. Wagelies, D.G. Fraser, M.C. Payne, M.H. Lee and V. Milan (1995) *Phys. Rev. B* **52**, 10833.

91. H. Papp and B. Egersdörfer, private communication;
    B. Egersdörfer (1993) PhD-Thesis, Ruhr-Universität Bochum.

92. G. Pacchioni and P.S. Bagus (1993) in H.-J. Freund and E. Umbach (eds.) *Adsorption on Ordered Surfaces of Ionic Solids and Thin Films*, Springer Series in Surface Science Vol. 33, Springer Verlag, Heidelberg, p.180.

93. a.) K. M. Neyman and N. Rösch (1992) *J. Chem. Phys.* **168**, 267;
    b.) K. M. Neyman and N. Rösch (1993) *Surf. Sci.* **297**, 223;
    c.) K. M. Neyman and N. Rösch (1993) *Chem. Phys.* **177**, 561.

94. C. Pisani, R. Dovesi, R. Nada and S. Tamiro (1989) *Surf. Sci.* **216**, 267.

95. H.-J. Freund and M. Neumann (1988) *Appl. Phys. A* **47**, 3.

96. G. Pacchioni, G. Cogliandro and P.S. Bagus (1991) *Surf. Sci.* **255**, 344;
    G. Pacchioni, P.S. Bagus (1992) in G. Pacchioni, P.S. Bagus and F. Parmigiani

100

(eds.) *Cluster Models for Surface and Bulk Phenomena*, NATO ASI Series, Series B: Physics, Vol. 283, Plenum, New York, p. 305.

97. M. Pöhlchen and V. Staemmler (1992) *J. Chem. Phys.* **97**, 2583.

98. G. Blyholder (1964) *J. Phys. Chem.* **68**, 2772.

99. A. Freitag, V. Staemmler, D. Cappus, C.A. Ventrice Jr., K. Al-Shamery, H. Kuhlenbeck and H.-J. Freund (1993) *Chem. Phys. Lett.* **210**, 10.

100. a) N.D.S. Canning and M.A. Chesters (1983) *J. Electron Spectrosc. Relat. Phenom.* **30**, 247;

    b) J. Rolfe (1968) *J. Chem. Phys.* **49**, 963.

101. J.H. Lunsford, X. Yang, K. Haller, J. Laane, G. Mestl and H. Knözinger (1993) *J. Phys. Chem.* **97**, 13810.

102. F.A. Müller, G.L. Carlton and W.B. White (1959) *Spectrochim. Acta* **15**, 709; W.E. Hobbs (1958) *J. Chem. Phys.* **28**, 1220.

103. P.J.M. Carrott and N. Sheppard (1983) *J. Chem. Soc. Farad. Trans.* **79**, 2425.

104. A.A. Davydov, Y.M. Shchekochikhin and N.P. Keier (1972) *Kinet. Katal.* **13**, 1088.

105. I.E. Wachs, *Catal. Today*, in press.

106. A. Zecchina, G. Spotoy and G. Ghiotti (1992) *J. Mol. Catal.* **74**, 175.

107. M. Bender, I.N. Yakovkin and H.-J. Freund (1996) *Surf. Sci.*, in press.

108. H. Kadowaki, H. Takei and K. Motoya (1995) *J. Phys.: Condens. Matter* **7**, 6869 and references therein.

109. B. Adam (1991) *Diploma-Thesis*, Ruhr-Universität Bochum.

110. H. Isern and G. R. Castro (1989) *Surf. Sci.* **211/212**, 865.

111. H. Pfnür, C. Schwennicke and J. Schimmelpfennig (1993) in H.-J. Freund and E. Umbach (eds.) *Adsorption on Ordered Surfaces of Ionic Solids and Thin Film*, Springer Series in Surface Sciences, Vol. 33, Springer Verlag, Heidelberg, p. 124.

112. Th. Bertrams, F. Winkelmann, Th. Uttich, H.-J. Freund and H. Neddermeyer (1995) *Surf. Sci.* **331-333**, 1515.

113. J. Libuda (1996) PhD-Thesis, Ruhr-Universität Bochum.

114. H.-J. Freund, B. Dillmann, D. Ehrlich, M. Haßel, R.M. Jaeger, H. Kuhlenbeck, C.A. Ventrice, F. Winkelmann, S. Wohlrab, C. Xu, Th. Bertrams, A. Brodde and H. Neddermeyer (1993) *J. Mol. Catal.* **82**, 143.

115. F. Winkelmann, S. Wohlrab, J. Libuda, M. Bäumer, D. Cappus, M. Menges, K. Al-Shamery, H. Kuhlenbeck and H.-J. Freund (1994) *Surf. Sci.* **307-309**, 1148.

116. S. Wohlrab, F. Winkelmann, J. Libuda, M. Bäumer, H. Kuhlenbeck and H.-J. Freund, *Adsorption on Epitaxial Oxide Films as Model Systems for Heterogeneous Catalysis* in Springer Proceedings in Physics, in press.

117. J. Libuda, A. Sandell, M. Bäumer and H.-J. Freund (1995) *Chem. Phys. Lett.* **240**, 429.

118. M. Bäumer, J. Libuda, A. Sandell, F. Winkelmann, H.-J. Freund, G. Graw, Th. Bertrams and H. Neddermeyer (1995) *Ber. Bunsenges., Phys. Chem.* **99**, 1381.

119. A. Sandell, J. Libuda, P.A. Brühwiler, S. Andersson, M. Bäumer, A.J. Maxwell, N. Mårtensson and H.-J. Freund, *J. Vac. Sci. Technol. A*, in press.

120. A. Sandell, J. Libuda, P. Brühwiler, S. Andersson, A.J. Maxwell, M. Bäumer, N. Mårtensson and H.-J. Freund (1995) *J. Electr. Spectr. Rel. Phen.* **76**, 301.

121. A. Sandell, J. Libuda, M. Bäumer and H.-J. Freund (1996) *Surf. Sci.* **346**, 108.

122. J. Libuda, M. Frank, A. Sandell, S. Andersson, P.A. Brühwiler, M. Bäumer, N. Mårtensson and H.-J. Freund, *Springer Proceedings in Physics*, accepted.

123. A. Sandell, J. Libuda, P.A. Brühwiler, S. Andersson, M. Bäumer, A.J. Maxwell, N. Mårtensson and H.-J. Freund *Phys. Rev. B*, submitted.

124. U.J. Katter, T. Hill, T. Risse, H. Schlienz, M. Beckendorf, T. Klüner, H. Hamann and H.-J. Freund, *J. Phys. Chem.*, submitted.

125. J. Heidberg and D. Meine (1993) *Ber. Bunsenges. Phys. Chem.* **97**, 211.

126. A. Zecchina, D. Scarano, S. Bordiga, G. Ricchiardi, G. Spoto and F. Geobaldo (1996) *Catal. Today*, **27**, 403.

127. M. Henzler, A. Stock and M. Böl (1993) in H.-J. Freund and E. Umbach (eds.) *Adsorption on Ordered Surfaces of Ionic Solids and Thin Films*, Springer Series in Surface Science, Vol. 33, Springer Verlag, Heidelberg.

128. K.M. Schröder, F. Schäfer, J. Wollschläger and M. Henzler, *Surf. Sci.* submitted.

129. C. Schwennicke, J. Schimmelpfennig and H. Pfnür (1993) *Surf. Sci.* **293**, 57.

130. P.J. Chen and D.W. Goodman (1994) *Surf. Sci. Lett.* **312**, L767.

131. Y. Wu, H.-S. Tao, E. Garfunkel, T.E. Madey and N.D. Shinn (1995) *Surf. Sci.* **336**, 123.

132. Y. Wu, E. Garfunkel and T.E. Madey (1996) *J. Vac. Sci. Technol. A* **14**, 1662.

133. S. Stempel, PhD-Thesis, Ruhr-Universität Bochum, in preparation.

134. J.E. McDonald and J.G. Eberhart (1965) *Trans. Met. Soc. AIME* **233**, 512.

135. D. Chatain, I. Rivollet and N. Eustathopoulos (1986) *J. Chim. Phys.* **83**, 561; (1987) *J. Chim. Phys.* **84**, 201.

136. E. Bauer (1958) *Zeitschrift für Kristallographie* **110**, 372.

137. J. Wollschläger, J. Falta and M. Henzler (1990) *Appl. Phys. A* **50**, 57.

138. P.R. Pukite, C.S. Lent and P.I. Cohen (1985) *Surf. Sci.* **161**, 39; C.S. Lent and P.I. Cohen (1984) *Surf. Sci.* **139**, 121.

139. G. Beitel, K. Markert, J. Wiechers, J. Hrbek and R.J. Behm (1993) in H.-J. Freund, E. Umbach (eds.), *Adsorption on Ordered Surfaces of Ionic Solids and Thin Films* Springer Series in Surface Science, Vol. 33, Springer-Verlag, Heidelberg, p. 71.

140. A.F. Hollemann and E. Wiberg (1985) *Lehrbuch der Anorganischen Chemie*, de Gruyter, Berlin.

141. M.G. Mason (1983) *Phys. Rev. B* **27**, 748.

142. G.K. Wertheim (1987) *Z. Phys. B* **66**, 53.

143. G.K. Wertheim (1989) *Z. Phys. D* **12**, 319.

102

144. G.K. Wertheim, S.B. DiCenzo and D.N.E. Buchanan (1986) *Phys. Rev. B* **33**, 5384.

145. F.A. Marks, I. Lindau and R. Browning (1990) *J. Vac. Sci. Technol. A* **8**, 3437.

146. K. Schönhammer and O. Gunnarsson (1978) *Z. Phys. B* **30**, 297.

147. K. Schönhammer and O. Gunnarsson (1977) *Solid State Commun.* **23**, 691.

148. S.B. DiCenzo and G.K. Wertheim (1985) *Comm. Solid State Phys.* **11**, 203.

149. H.-J. Freund in G. Ertl, H. Knözinger and J. Weitkamp (eds.) *Handbook of Heterogenous Catalysis* Part A, Chapter 5.1, Section 5.1.1 Principles of Chemisorption, in press.

150. D.A. King and D.P. Woodruff (eds., 1990) *Chemisorption Systems* The Chemical Physics of Solid Surfaces and Heterogeneous Catalysis, Vol. 3, Part A, Elsevier.

151. N. Mårtensson and A. Nilsson (1995) in W. Eberhardt (ed.) *Applications of Synchrotron Radiation* Springer Series in Surf. Science Vol. 35, Springer.

152. H.-J. Freund and M. Neumann (1988) *Appl. Phys. A* **47**, 3.

153. J.N. Andersen, D. Hennig, E. Lundgren, M. Methfessel, R. Nyholm and M. Scheffler (1994) *Phys. Rev. B* **50**, 17525.

154. J.N. Andersen, M. Quarford, R. Nyholm, S.L. Sorensen and C. Wigren (1991) *Phys. Rev. Lett.* **67**, 2822.

155. O. Björneholm, A. Nilsson, H. Tillborg, P. Bennich, A. Sandell, B. Hernnäs, C. Puglia and N. Mårtensson (1994) *Surf. Sci.* **315**, L983.

156. B.G. Frederick, G. Apai and T.N. Rhodin (1987) *J. Am. Chem. Soc.* **109**, 4797.

157. X. Guo and J.T. Yates Jr. (1998) *J. Chem. Phys.* **90**, 6761.

158. E.W. Plummer, W.R. Salanek and J.S. Miller (1978) *Phys. Rev. B* **18**, 1673.

159. H.-J. Freund and E.W. Plummer (1981) *Phys. Rev. B* **23**, 4859.

160. H.-J. Freund, E.W. Plummer, W.R. Salaneck and R.W. Bigelow (1981) *J. Chem. Phys* **75**, 4275.

161. J.N. Andersen et al., unpublished results.

162. J.C. Fuggle, E. Umbach, D. Menzel and K. Brundle (1978) *Solid State Commun.* **27**, 65.

163. K. Schönhammer and O. Gunnarsson (1980) *Phys. Scr.* **21**, 575.

164. O. Gunnarsson and K. Schönhammer (1978) *Phys. Rev. Lett.* **41**, 1608.

165. E. Umbach (1982) *Surf. Sci.* **117**, 482.

166. A. Nilsson and N. Mårtensson (1989) *Phys. Rev. B* **40**, 10249.

167. H. Tillborg, A. Nilsson and N. Mårtensson (1993) *J. Electr. Spectr. Relat. Phen.* **62**, 73.

168. P.S. Bagus and M. Seel (1981) *Phys. Rev. B* **23**, 2065.

169. A. Nilsson, N. Mårtensson, S. Svensson, L. Karlsson, D. Nordfors, U. Gelius and H. Ågren (1992) *J. Chem. Phys.* **96**, 8770.

170. A. Sandell, J. Libuda, P.A. Brühwiler, S. Andersson, M. Bäumer, A.J. Maxwell, N. Mårtensson and H.-J. Freund, in preparation.

171. J. Bustad, C. Enkvist, S. Lunell and S. Svensson (1995) *J. Electron Spectrosc. Relat. Phen.* **70**, 233.

172. T. Porwol, G. Dömötör, I. Hemmerich, J. Klinkmann, H.-J. Freund and C.-M. Liegener (1994) *Phys. Rev. B* **49**, 10557.

173. J. Klinkmann, D. Cappus and H.-J. Freund (1995) *J. Electr. Spectrosc. Relat. Phenom.* **72**, 37.

174. J. Stöhr (1991) *NEXAFS Spectroscopy* Springer Series in Surf. Sci., Vol. 25 Springer-Verlag, Heidelberg.

175. U. von Barth and G. Grassmann (1982) *Phys. Rev. B* **25**, 5150.

176. A. Nilsson and N. Mårtensson (1995) *Physica B* **209**, 19.

177. A. Nilsson, O. Björneholm, E.O.F. Zdansky, H. Tillborg, N. Mårtensson, J.N. Andersen and R. Nyholm (1992) *Chem. Phys. Lett.* **197**, 12.

178. O. Björneholm, A. Nilsson, E.O.F. Zdansky, A. Sandell, B. Hernnäs, H. Tillborg, J.N. Andersen and N. Mårtensson (1992) *Phys. Rev. B* **46**, 10353.

179. H.F.J. van't Bilk, J.B.A.D. van Zon, T. Huizinga, J.C. Vis and D.C. Koningsberger (1983) *J. Phys. Chem.* **87**, 2264; (1985) *Am. Chem. Soc.* **107**, 3139.

180. F. Solymosi and M. Pásztor (1985) *J. Phys. Chem.* **89**, 4789.

181. P. Basu, D. Panayotov and J.T. Yates Jr. (1987) *J. Phys. Chem.* **91**, 3133; (1988) *J. Am. Chem. Soc.* **110**, 2074.

182. F. Solymosi and H. Knözinger (1990) *J. Chem. Soc. Faraday Transactions* **86**, 389.

183. D. N. Belton and S. J. Schmieg (1988) *Surf. Sci.* **202**, 238.

184. V. Nehasil, I. Stará and V. Matolín (1995) *Surf. Sci.* **331-333**, 105.

185. M. Rebholz, R. Prins and N. Kruse (1991) *Surf. Sci.* **259**, L797; (1992) *Surf. Sci.* **269/270**, 293.

186. V. Matolín, K. Mâsek, M.H. Elyakhloufi and E. Gillet (1993) *J. Catal.* **143**, 492.

187. A. de Koster and R.A. van Santen (1990) *Surf. Sci.* **233**, 366.

188. D. B. Almy, D. C. Foyt and J. M. White (1977) *J. Electron Spectrosc. Relat. Phen.* **11**, 129.

189. J. Paul and F. M. Hoffmann (1986) *J. Phys. Chem.* **21**, 5321.

190. J.G. Chen, J.E. Crowell and J.T. Yates Jr. (1986) *J. Phys. Chem.* **84**, 5906.

191. V. Coustet and J. Jupille (1994) *Surf. Sci.* **309**, 309; (1994) *Surf. Interface Anal.* **22**, 280.

192. B.G. Frederick, G. Apai and T.N. Rhodin (1991) *Surf. Sci.* **244**, 67.

193. M.A. Schildbach and A.V. Hamza (1993) *Surf. Sci.* **282**, 306.

194. A. Ludviksson, K.H. Ernst, R. Zhang and C.T. Campbell (1993) *J. Catal.* **141**, 380.

195. N. Kruse and A. Gaussmann (1993) *J. Catal.* **144**, 525.

196. M.H. El-yakhloufi and E. Gillet (1993) *Catal. Lett.* **17**, 11.

197. H.A. van der Vegt, H.M. van Pinxteren, M. Lohmeier, E. Vlieg and J.M.C. Thornton (1992) *Phys. Rev. Lett.* **68**, 3335.

198. M. Horn-von Hoegen, M. Pook, A. Al-Falou, B.H. Müller and M. Henzler (1993) *Surf. Sci.* **284**, 53.

199. H. Wolter, M. Schmidt and K. Wandelt (1993) *Surf. Sci.* **298**, 173.

200. S. Esch, M. Hohage, T. Michely and G. Comsa (1994) *Phys. Rev. Lett.* **72**, 518.

201. H.-J. Freund, H. Kuhlenbeck (1995) in W. Eberhardt (ed.) *Applications of Synchrotron Radiation,* Springer Series in Surface Science, Vol. 35, Springer, p. 9.

202. J.E. Reutt, L.S. Wang, Y.T. Lee and D.A. Shirley (1986) *Chem. Phys. Lett.* **126**, 399.

203. J.H. Darling and J.S. Ogden (1972) *Inorganic Chemistry* **11**, 666; (1972) *J. Chem. Soc. Dalton Trans.,* 2496.

204. P. Kuendig, M. Moskovits and G.A. Ozin (1972) *Can. J. Chem.* **50**, 3587; (1972) *J. Mol. Struct.* **14**, 137.

205. H. Huber, P. Kuendig, M. Moskovits and G.A. Ozin (1977) *Nature* **235**, 98.

206. L.-L. Sheu, H. Knötzinger and W.M.H. Sachtler (1989) *J. Am. Chem. Soc.* **111**, 8125.

207. Z. Zhang, H. Chen and W.M.H. Sachtler (1991) *J. Chem. Soc. Faraday Trans.* **87**, 1413.

208. Z. Zhang, F.A.P. Cavalcanti and W.M.H. Sachtler (1992) *Catal. Lett.* **12**, 157.

209. P.A. Hintz and K.M. Ervin (1994) *J. Chem. Phys.* **100**, 5715.